FAIZA SUMMER

Development and optimization
of flow electrode capacitor technology

TARTU ÜLIKOOL
UNIVERSITAS TARTUENSIS
1632

DISSERTATIONES TECHNOLOGIAE UNIVERSITATIS TARTUENSIS

65

FAIZA SUMMER

Development and optimization of flow electrode capacitor technology

Institute of Technology, Faculty of Science and Technology, University of Tartu, Estonia

Dissertation was accepted for the commencement of the degree of Doctor of Philosophy in Engineering and Technology on 31st March, 2022 by the Council of the Institute of Technology, Faculty of Science and Technology, University of Tartu

Supervisors: Janno Torop, PhD
                Researcher, Institute of Technology, Faculty of Science and Technology, University of Tartu, Estonia

                Veronika Zadin, PhD
                Professor of Simulation in Materials Science and Engineering, Institute of Technology, Faculty of Science and Technology, University of Tartu, Estonia

                Alvo Aabloo, PhD
                Professor of Polymeric Materials and Materials Science, Institute of Technology, Faculty of Science and Technology, University of Tartu, Estonia

Reviewer: Silver Sepp, PhD
                Research Fellow,
                Institute of Chemistry, Faculty of Science and Technology, University of Tartu, Estonia

Opponent: Pekka Peljo, PhD
                Associate Professor, Materials Engineering
                University of Turku, Finland.

Commencement: Auditorium 121, Nooruse 1, Tartu, Estonia, 14:15 on May 10th, 2022

Publication of this thesis is granted by the Institute of Technology, University of Tartu.

ABSTRACT

Electrical energy storage (EES) systems are the key elements in building sustainable energy technologies. Modern electrochemical energy storage devices like batteries and supercapacitors primarily address small-scale storage, such as consumer and micro-electronics. Batteries are reliable when applications require high energy density, while supercapacitors are used in high power density required applications. The electrochemical flow capacitor (EFC) was first introduced in 2011, potentially overcoming supercapacitors' low energy density limitations. The EFC energy storage adopts its characteristics from both flow batteries and supercapacitors. The similarity of its architecture to the flow batteries supports the scalability of energy capacity, while the super-capacitive charge storage mechanism offers a high power density and long lifecycle. The distinctive property of this technology is the use of nanoscaled carbon particles suspended in the electrolyte, also known as the flow electrode (FE). The fast charge/ discharge operations make it a potential candidate for grid-scale energy and support integration with the intermittent energy source. However, the flowing nature of the electrode makes the energy storage process more complex than in the solid electrodes. The suspended carbon's electric double layer (EDL) charging in the presence of an electrolyte varies extensively with its flow conditions, e.g., viscosity, flow rate, and channel geometry.

This thesis presents experimental and simulations efforts to optimize the EFC device design. The flow electrodes in the experiments consist of low concentration carbonaceous material: 5 mg/ml in 0.1 M Na_2SO_4 (aqueous), and 3% viscosity enhancer carboxymethyl cellulose sodium salt (CMC-Na). The electrochemical characterization was performed for the prepared flow electrodes at a flow rate of 2 ml/min in a hermetically sealed EFC module. The main components of the EFC module were the 5 mm wide × 120 mm long stainless-steel current collector channels in which the flow electrodes were allowed to charge as external polarization was applied. Both channels were separated by an ion-conducting membrane, ensuring the flow electrode's secluded path. The optimization of the EFC design is conducted by using the finite element method (FEM). The numerical method for the design optimization was based on Johnson and Newman's macroscopic approach of desalting porous carbon electrodes. In each flow channel, the high surface area carbon electrode was allowed to adsorb the electrolytic ions (Na^+ and $[SO_4]^{2-}$) from the vicinity to form instant EDL. The optimization of EFC design (size and shape) and utilization of the carbon electrodes was studied using the homogenized phases of electrode and electrolyte in the symmetric and asymmetric configurations of the flow channels. The particle tracking-based stochastic model studied the electrode charging in a flow channel individually on a particle scale. The method was well equipped to use the physical properties of the carbon electrode, for example, the size and concentration. Both modeling methods were validated with the measured experimental performance of flow electrodes in terms of current and charge. Furthermore, the estimation of the modeling parameters was performed for each method individually to match the experiment and modeling results with minimum error.

CONTENTS

LIST OF PUBLICATIONS

I. Torop, J.; Summer, F.; Zadin, V.; Koiranen, T.; Jänes, A.; Lust, E.; Aabloo, A. Low concentrated carbonaceous suspensions assisted with carboxymethyl cellulose as electrode for electrochemical flow capacitor. *Eur. Phys. J. E* **2019**, *42*, http://doi.org/10.1140/epje/i2019-11766-2.

II. Summer, F.; Zadin, V.; Nakshatharan, S.S.; Aabloo, A.; Torop, J. Optimization of electrochemical flow capacitor (EFC) design via finite element modeling. *J. Energy Storage* **2020**, *29*, 101304, http://doi.org/10.1016/j.est.2020.101304.

III. Summer, F.; Torop, J.; Aabloo, A.; Kyritsakis, A.; Zadin, V. Particle dynamics-based stochastic modeling of carbon particle charging in the flow capacitor systems. *Appl. Sci. 2022, Vol. 12, Page 1887* **2022**, *12*, 1887, http://doi.org/10.3390/APP12041887.

AUTHORS CONTRIBUTION

The author of this thesis is responsible for simulation research in all phases.

In **publication I**, the author developed the electrochemical model, conducted simulation and analysis. The author was responsible for writing the simulation part of the paper.

In **publication II**, the author was responsible for model designing, simulations, results analysis, and conclusions. The author was in charge of writing the paper and was the corresponding author.

In **publication III**, the author simulated, analyzed the results, and took the lead for paper writing.

ABBREVIATIONS AND SYMBOLS

RES	Renewable energy sources
EFC	Electrochemical flow capacitor
FC/FE	Flow capacitor/Flow electrode
FEM	Finite element method
PDE	Partial differential equation
EDL	Electrical double layer
DL	Double layer
EDLC	Electric double layer capacitor
EIS	Electrochemical impedance spectroscopy
CV	Cyclic voltammetry
EIS	Electrochemical impedance spectroscopy
CCs	Current collectors
F	Faraday constant (96487 C mol^{-1})
R	Universal gas constant (8.314 J (mol K)$^{-1}$)
CMC-Na	Carboxymethyl cellulose sodium salt
OLC	Onion like carbon
BOBYQA	Bound optimization by quadratic approximation
OT	Optimality tolerance
OF	Objective function
SPs	Super particles
PIC	Particle-in-cell
MD	Molecular dynamics
a_{spec}	Specific area of an electrode (m^{-1})
c_i	Ionic concentration (mol m^{-3})
D_i	Diffusion coefficient (m^2 s^{-1})
T	Absolute Temperature (K)
z_i	Ionic charge number
N_i	Ionic flux density (mol (m^{2}s)$^{-1}$)
j_1	Electronic current density in the electrode (A m^{-2})
j_2	Ionic current density in electrolyte (A m^{-2})
k	Ionic conductivity (mS cm^{-1})
σ	Electronic conductivity (mS cm^{-1})
d_p	Diameter of carbon particle
V_p	Volume of carbon particle
m_{cp}	Mass of single carbon particle
β_{Na}	Number of Na ions per carbon particle
D_{sp}	Diameter of a superparticle
V_{sp}	Volume of a superparticle
V_{SP}	Total volume of superparticles

D_{IA}	Interaction diameter of superparticles
n_{NPS}	Average number of carbon particles in a superparticle
$needed_{NSP}$	Number of SPs needed
$actual_{NSP}$	Number of superparticles actually used in each channel

Subscripts and superscripts

$+$	For positive ion from electrolyte (Na^+ in this case)
$-$	For negative ion from electrolyte ((SO_4)$^{2-}$ in this case)

LIST OF TABLES

LIST OF FIGURES

LIST OF FLOWCHARTS

1. INTRODUCTION

The growing emphasis on sustainable energy production and use has created a significant impetus for developing novel energy conversion and storage approaches. To harness the renewable energy sources (RES) like wind and solar requires advancements of the associated energy storage technologies to overcome grid instability and poor reliability. The most important parameters associated with energy storage technologies are energy density, power density, charge/discharge characteristics, life cycles/lifetime, and round-trip efficiency [1]. For the intermittent renewable sources, the technologies delivering high power density in a short response time are more feasible for grid-scale storage [2, 3]. Batteries are closed systems recognized because of their high energy density. The anode and cathode in a battery are the charge-transfer medium and take an active role in the redox reaction as "active masses" [4]. The lithium-ion battery is a specific electrochemical battery with a high specific energy. It has been adopted as the core energy source for consumer electronics, electric vehicles, and energy storage devices [5]. Unlike static [6] and solid batteries [7], flow batteries [6, 8] allow control of the capacity and energy characteristics, as capacities, in this case, are influenced by the type of electrolyte and the size of the electrode reservoir used. Several chronic problems preventing commercialization have yet to be solved, including cost reductions, long life spans, and a more compact system. However, supercapacitors provide high power density, fast charge-discharge, and long service life compared to batteries. The specific capacitance (C) of a super-capacitor is defined as $C = {Q}/{V}$, where Q is the stored charge on the electrode per unit mass and V is the operating voltage window. **Table 1** gives a summary of different types of energy storage devices with mechanisms.

Electrochemical flow-electrode capacitor (EFC) is an energy storage technology first introduced in 2012. It possesses significant advantages of super-capacitors and flow batteries, the high-power density and long cycle lifetime of supercapacitors [9], and the scalable energy capacity of flow batteries [10]. The unique aspect of this concept is using a flowable electrode-electrolyte suspension called slurry for capacitive energy storage. Fundamentally, the EFC is based on the same charge storage mechanism as supercapacitors, where reversible polarization is the source of the EDL formation by counter-balancing the porous electrode's surface charges. The prototype system could store energy with a coulombic efficiency of more than 98% [10]. The working principle can be complex and affected by many different aspects of materials choice, device design, the interactions within materials, and its effect on the device [10, 11]. EFC device can be operated under static conditions and continuous flow mode [12].

The electrochemical and rheological assessment of slurry electrodes performed for carbon particles with different shapes, sizes, and concentrations show that the intermediate particle size is more favorable for electronic charge transfer through the particles [13, 14]. Aqueous [14, 15], organic [16], ionic liquid [17, 18], and polymer-based electrolytes [19–21] can be utilized in supercapacitors and

batteries. Each electrolyte class presents distinctive properties that may be promising for EFC performance. The function of the aqueous electrolyte is to balance the surface charge developed in the electrode. Solubility, ion size, chemical stability, and oxidation state of the salt affect EFC performance. In addition, also the ionic conductivity of the salt, electronic conductivity, chemical stability, and viscosity of the aqueous media affect EFC performance [22].

Table 1. Different energy storage devices with the working mechanism.

Types of device		Charge storage mechanism	Electrode material	Benefits and drawbacks	Ref.
Lead-acid battery		Chemical kinetics	$PbSO_4/H_2SO_4$	Start-up power, Poor energy density.	[23]
Lithium-ion battery		Intercalation, redox reactions	Graphite & Lithium base layered oxide.	High energy density, portable, Depletable elements in most applications.	[23, 24]
Flow Battery		Redox reactions	Graphite felt, V_2O_5 in sulfuric acid (H_2SO_4)	Independent scalability, very long-life cycle, low system efficiency.	[25, 26]
Electrochemical double layer (EDL) capacitor		non-Faradaic process	Carbon black, carbon beads	Good cycling stability and rate capability, low energy density, and specific capacitance.	[27, 28]
Pseudo-capacitor		Faradaic process, Surface redox reaction	Redox metal oxide or redox polymer	High specific capacitance, relatively high energy density, relatively high-power density, relatively low-rate capability.	[4, 29, 30]
Hybrid capacitor	Sym-metric	Redox reaction plus EDL	Redox metal oxide /carbon or redox polymer/carbon	High energy density, moderate cost, and stability.	[31–33]
	Asym-metric	Anode: redox reaction, cathode: EDL	Anode: pseudo capacitance materials, cathode: carbon	High energy density and power density and good cyclability.	[31, 34]
	Hybrid (Battery-like)	Anode: Lithiation/de-lithiation cathode: EDL	Anode: Li-insertion material, cathode: carbon	High energy density, high cost, and requires electrode material capacity match.	[31, 33, 35]

15

Slurry preparation protocols readily improve the conductivity by 57% for the same composition of electrode and electrolyte [36]. Depending on the mixing method, even when sufficient time was allowed for mixing (i.e., 15 min), capacity differences as high as 91.5% have been found for the same electrode composition [36]. The electrochemical impedance spectroscopy (EIS) model is used to analyze the effect of the slurry's flow rate on its intrinsic properties like electronic conductivity and diffusivity. The electrical conductivity changes slightly from 1.30 S/m at 50 mL/min to 1.28 S/m at 250 mL/min for the same composition slurry, pointing to the inter-particle percolation networks near the wall are not altered much by changes in the flow rates in this range [37]. However, a significant increase in the electronic diffusivity is observed from 2.13×10^{-8} m^2/s at 50 mL/min to 2.79×10^{-8} m^2/s at 250 mL/min, suggesting the reduction in specific capacitance of the slurry associated with underutilization of micropores in the activated carbon particles at higher flow rates [37]. To study the electronic conductivity of the flowable electrode, a dilute slurry combined with a gravity-affected fluidized bed was introduced (named combined electrode). Lower than expected values of electronic conductivity in the gravity-affected fluidized bed electrodes are because of the unclear transport mechanism [38].

Prediction of the performance of such electrochemical systems is essential as modeling can be a useful avenue in the search for design improvements and optimization of basic parameters. The rudimentary mathematical modeling approach is based on macroscopic balance equations of advection-diffusion heat and mass transfer [39]. In a non-flowing electrode system, the advection-diffusion of surface charge is dominant in the cell for the different ratios of the ionic and electronic conductivities [40, 41]. While under the flow conditions, the particle's motion and the mutual contact mechanism put a considerable strain on the electrical conductivity of the bulk material [42].

Experiments and simulations support each other in describing different charging mechanisms by going beyond the traditional view of charging by counter-ion adsorption. It is shown that charging almost always involves ion exchange (swapping of co-ions for counter-ions) and rarely occurs by counter-ion adsorption alone [43]. A generalized electrical circuit model was developed to study the charge transfer among the particles, which accounts for the dynamically varying configuration of the particle network. The charge exchange and particle dynamics are solved simultaneously to study the particle-particle interaction effect on the charge transport in the slurry electrode. The simulations also demonstrate that particle clusters' formation in the flow is important for effective charge transport [44]. Modeling the composition of electrodes and electrolyte shows the low polarizability and underutilization of the electrodes [45, 46]. Modeling efforts also account for using slurry's physical properties, cell dimensions, conductivities, and faradic/ non-faradic kinetics in context to flow battery and flow electrode capacitor [47, 48].

1.1 Motivation and Aim

Electrochemical flow capacitor is the hybrid of the flowable slurry electrode and capacitive energy storage architecture. The design of the EFC is critically essential to facilitate the flowing nature of charging electrodes. The electrical conductivity of a suspension electrode portrays the connectivity of active material and pronounced percolation path. The static mode of operation enhances the efficient charge transfer, while in dynamic mode, the network of active particles collapses, forming large voids, which can inflate the resistance and inefficient charge transfer. Particle dynamics within the flow channel strongly affect the charge transport and storage within the bulk of suspension electrodes. The dominance of these localized effects of particle networks is determined by the flow rate and the geometrical design of the flow channels. The EFC design should mitigate clogging, maximize the overall performance, and operate in several modes (static and continuous) when scaled up. A thorough understanding of these variables is critical to guide system design and operation strategies.

Motivated by EFC technology's needs and current state, this thesis aimed to investigate the charging of carbon-based flow electrodes in the circular-shaped flow channel architecture. Carbon-based flow electrodes in an aqueous electrolyte medium were used to evaluate its energy storage capacity at a low flow rate. The effect of flow channel size and shape was studied using the finite element models to extract the additional data and improve the understanding of the electrodes charging behavior in a flow channel. The models were parametrized using the experimental study and later used to test their sensitivity for the charging activity inside the flow channel for three different designs. In one model, the carbon electrodes were presented as a homogenized phase, and in the other, carbon electrodes were spherical particle-based. The two models are designed to study carbon electrodes' capacitive charging.

The coupling of the EFC experimental study with the predictive approach of modeling not only provides a deeper understanding of the technology but also assists in recognizing the parameters limiting its performance and benchmarking of the optimal design. The results presented in this thesis are specific to an energy-storing flow capacitor, the conclusions can be implemented for other flow electrode technologies like flow electrode capacitive deionization. Such modeling techniques can later be adapted for the scalability of the infrastructures using flow electrodes.

1.2 Structure of this work

The results of the EFC study are published in the following papers:

Publication I: Experimental study was conducted with the carbon-based slurry electrodes suspended in Na_2SO_4 aqueous medium. The slurry was charged at 2ml/min flow rate in the symmetrically designed circular-shaped flow channel

prototype. Experimental results were combined with time-dependent FEM simulations to study the current density distribution and overall efficiency within the device's flow channel.

Publication II: The FEM model based on Newman's theory for the porous electrode is used to optimize the slurry electrode parameters. The study was conducted for three different geometrical design arrangements. The model investigates the effects of geometrical shape and depth of flow channels on the electronic current density distribution. The transport of electrolytic ions in the flow channels and the utilization of the electrode during the charging process were studied for each geometrical design. The asymmetric geometrical arrangement was also part of the study.

Publication III: The experiments were conducted for a specific slurry composition, and the results were compared with the model. This paper is based on the carbon particle-based slurry charging in a circular-shaped flow channel design. The study is conducted to understand the underutilization of carbon electrodes during the charging process. The model explains the efficiency of slurry charging by tracking the carbon particles cluster and their contact with the neighboring network for the charge transport throughout the slurry.
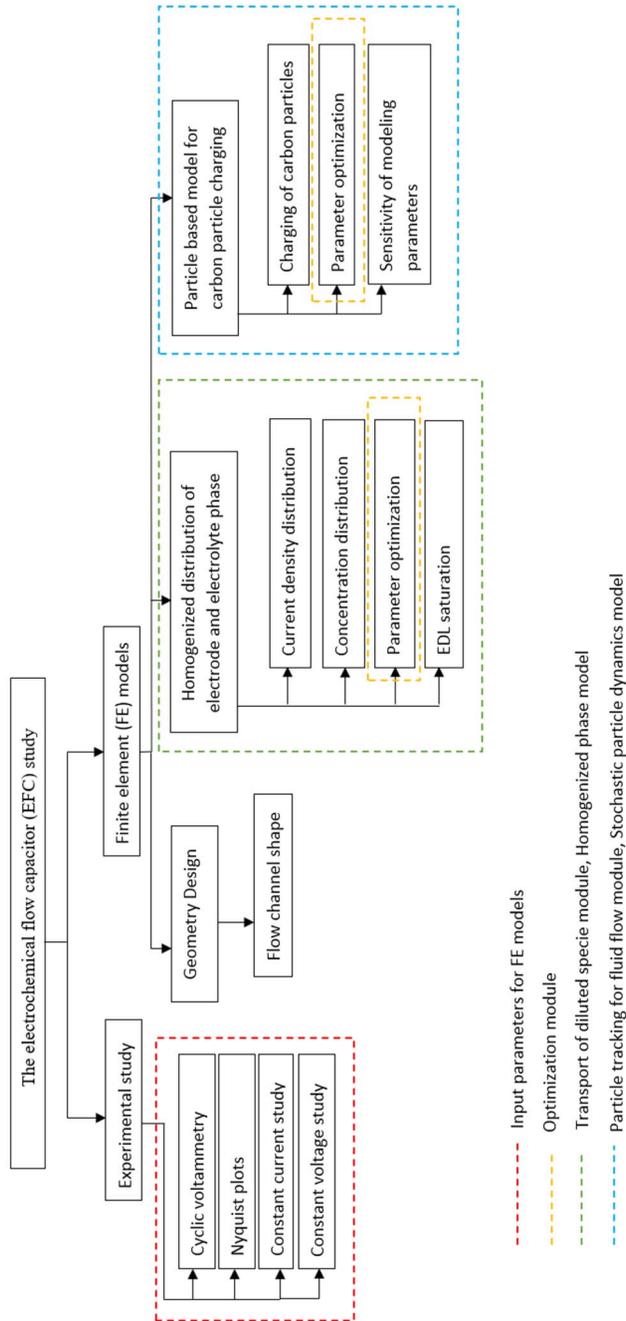
Flow chart 1. The scheme of study for this thesis work. Experiments were conducted for the specified system of slurry composition. The continuum modeling method (homogenized phase model) used the experimental values of the concentration and diffusion coefficient to optimize the design of the flow capacitor device. Physical properties of the carbon electrode from the slurry are used for the particle-based model of charging flow capacitor.

1.3 The Electrochemical Flow Capacitor

The electrochemical flow capacitor (EFC) design is essential to facilitate the flow of the slurry electrodes and maximize its performance efficiency. EFC cell consists of two flow channels to accommodate the charging and the flow of slurry electrodes and the membrane which separates the flow channels. **Figure 1** shows the closeup of the charging mechanism of the flow electrodes. The black spherical particles are carbon electrodes, and small red and blue spheres are depicted as electrolytic salt ions that form a double layer interface. The electrode is charged and discharged by the transfer of electrons due to the external polarization of the current collector. The function of the electrolytes in the slurry charging is to balance the charge developed in the electrode. The membrane isolates the channels and prevents shorting across the electrodes while allowing ions to move across the channel to maintain electroneutrality. The rapid adsorption of electrolytic ions on the electrode surface is due to their electrostatic interactions. It will enable EFC to hold high power density, long cycle lifetime but limited energy density leading to a large EFC size.
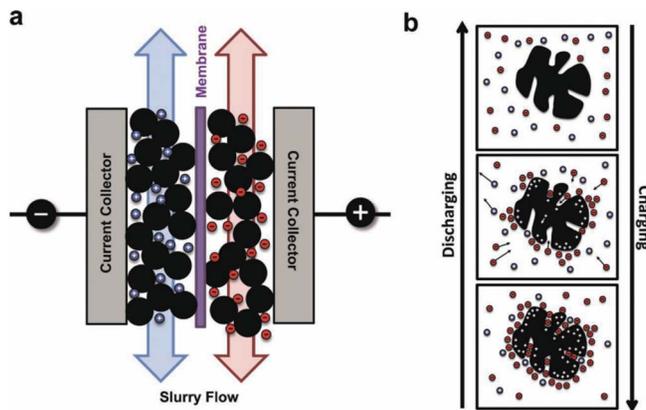
Figure 1 . Concept of the charge storage mechanism of the electrochemical flow capacitor (EFC). A carbon/electrolyte mixture (slurry) is pumped between two polarized current collectors for charging and discharging (a). Energy stored in the electric double layer (EDL): ions from the electrolyte counter-balance the surface charges of the polarized carbon particles (b). Discharge is accomplished by depolarizing the EDL [10].

1.3.1 Electric double-layer models

The formation of EDL is a physical surface process and is mainly influenced by the properties of the electrode. The buildup of positive (or negative) charge at the electrode and electrolyte solution interface is partially neutralized by gathering counter-ions in the solution through the action of Coulomb's force in a structured electric double layer. The interface structure always exhibits a behavior different

from the bulk electrolyte under external potential [49]. The thickness of the diffuse region in the electric double layer depends on the concentration of ions in the bulk solution: the lower the ion concentration, the thicker the diffuse layer. There are three different theories related to EDL formation: the Helmholtz parallel plate theory, Guoy-Chapman's (GC) diffuse charge theory, and Stern's double layer theory. According to the Helmholtz model, the variation of the potential of the double layer with distance into the solution is linear. In the GC model, the potential change is not linear but exponential. The Stern model combines the Helmholtz and GC theories to give the electric double layer model. The potential drop for each model is shown in **Figure 2**.
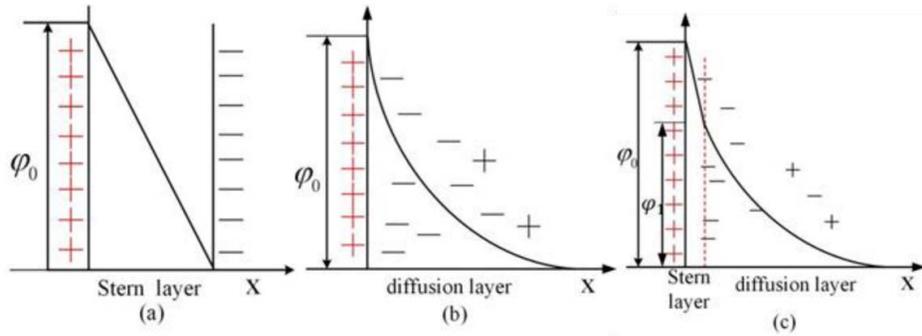
Figure 2. Potential variation of electric double layer (EDL) models. (a) Helmholtz model, (b) Gouy–Chapman model, (c) and the Gouy–Chapman–Stern model, respectively [50].

2. COMBINED COMPUTATIONAL AND EXPERIMENTAL INVESTIGATIONS

2.1 Materials for semi-solid electrodes

The overall performance of electrochemical capacitors is decided by both the electrode material and electrolyte used. Materials used in EDLCs are carbon aerogel, activated carbon, carbon fibers, and carbon nanotubes. The choice of electrode materials is related to the electric double-layer structure. Surface topography and electrodes modification affect ion accumulation at the electrode/electrolyte interface. For example, the higher surface curvature of carbon nanotubes at the interface is beneficial for the ion density per unit area [51]. Different simulation methods are proven effective at different scales, which has motivated efforts to combine multiple ways to simulate multiscale systems (**Figure 3**) [52].

Time scale / Length scale

Gaussian — quantum chemistry — $H\Psi = E\Psi$

CHARMM molecular dynamics — $F = ma$

kinetic Monte Carlo — $\exp(-\Delta E/kT)$

meso-scale — $f_i(x+v\Delta t, t+\Delta t) = f_i(x,t) + \Omega_i$

Fluent, COMSOL Abaqus — $\partial_t C_i + u \cdot \nabla C_i = D\nabla^2 C_i + R_i$ continuum
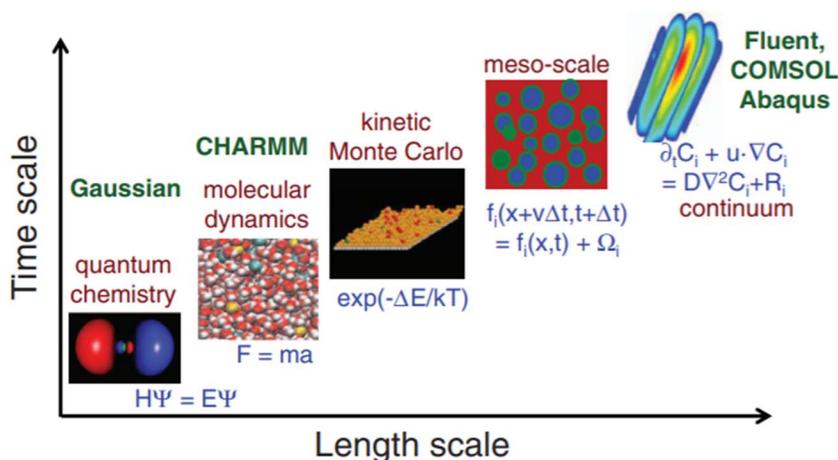
Figure 3. Approximate methods appropriate for the simulation of different time and length scales [52].

Molecular dynamics(MD) simulations provide the necessary insights into the capacitive performance and ions behavior at the interface of onion-like carbon (OLC) structure in various organic electrolytes. The large alkyl chains of cation from TBA-BF$_4$ lead to better separation of ions and counter-ions at the charged OLC particle surface and better charge screening [53]. The Finite Element (FE) simulations were conducted for Lithium-ion electrochemistry in flow batteries to observe the ionic flux, electronic current, and hydrodynamic flow. The developed models also explore other operational behavior of flow cells, including the effects of cell geometry, interfacial impedance, and semi-solid electrode transport limitations [54]. Electronic current and conductivity depend on the direct physical contact of the electrode particles or the hopping mechanism of electrons. The

Stokesian and circuit models use the particle's motion and their mutual contact to study their hydrodynamic interaction, and cluster formation affects the charge transport process in activated carbon electrodes [42]. The equivalent circuit models are capable of using 'flow capacitor' circuit elements instead of stationary charged media for EFC. The modified carbon slurry with carbon black as a conductive agent in the aqueous electrolyte uses the 'flow capacitor' circuit element model to approximate the EFC working behavior under static and flow conditions. The state of charge gradient shows the electrode's charging within 750 μm of the current collector when operated under flow conditions. The underlying cause points out the underutilization of the electrode material and high electrical resistance [55]. Various mathematical models based on Newman's porous carbon electrode desalting method [39] study the suspension electrodes and their transport process (diffusion, migration, convection) under different operating conditions [40, 41].

2.2 Materials and methods used

In all experiments, activated porous carbon (Vulcan XC 72R) was used as the electrode material. The characteristic properties of Carbon (Vulcan XC 72R) are given in **Table 2**. The aqueous Na_2SO_4 was used as an electrolyte. The mixture consists of carbonaceous material at a low concentration of 5 mg/ml, 0.1 M Na_2SO_4 and of 3% viscosity enhancer carboxymethyl cellulose sodium salt (CMC-Na). The porous carbon and CMC-Na were mixed with electrolyte to obtain a slurry electrode. The prepared carbonaceous suspension electrode material was kept in slurry reservoirs, and a peristaltic pump was used to mediate the flow-electrode material to the separation cell at the desired flow rates. The selected carbonaceous suspension portions observed can be considered static electrodes in a limited time frame.

Table 2. Properties of Carbon black (Vulcan XC 72R)

Properties of Carbon Vulcan XC 72R		
Average size of particles (nm)	50	[56]
BET surface area (m^2/g)	235	[57]
Bulk density (kg/m^3)	96.11	–

2.3 Testing cell device

The EFC cell consists of two symmetric stainless-steel tubes as flow channels. Along the flow direction of stainless-steel tubes, the current collectors have ablated edges facing the ion-conducting membrane separator. The uncharged slurry was introduced in the flow channels using a peristaltic pump and maintained at a specific flow rate during the charging. Each channel had a depth of 5 mm and

was separated by an ion (Na^+ and SO_4^{2-}) conducting membrane with a thickness of 150 μm. The EFC testing device in the experimental setup is shown in **Figure 4** [46].
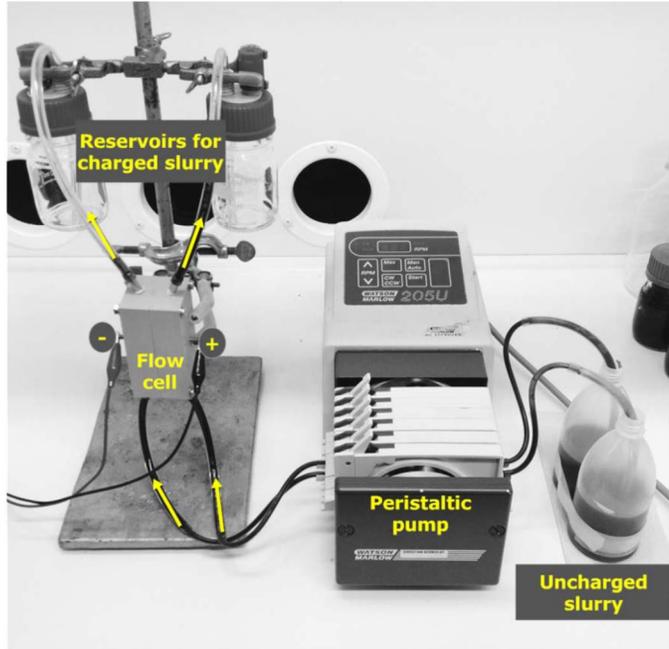
Figure 4. Photograph of circulating electrode flow capacitor cell and experimental setup for charging.

2.4 Homogenized phase models using Nernst Planck equation

Theoretical modeling of electrochemical processes is essential to understand the experimental results better. Considering the modeling of electrochemical energy storage devices, various categories have been suggested based on different aspects of the working principle. Continuum modeling method as a (Poisson-Nernst-Planck equation) homogenized phase models, Finite element modeling method (FEM), atomistic models (Monte Carlo, molecular dynamics), Quantum models (ab-initio quantum chemistry and Density Functional Theory), and simplified analytical models are a few of the valuable techniques. Each method has been developed to achieve various outcomes, and each displays multiple advantages and challenges.

In combination with experimental data, modeling is a powerful tool for advancing the developing technologies and for the intention of a detailed understanding of the processes in the materials and devices. The homogenized phase model allows investigating the charging/discharging dynamic of the electric

double-layer (EDL) capacitor. This continuum modeling approach treats the heterogeneous microstructure of the electrodes as homogeneous with some effective macroscopic properties determined from effective medium approximations and depending on porosity and specific area [39, 58]. The model allows the definition of effective diffusion coefficients for each type of ions separately within the electrode domain [59]. With the total charge storage capacity of the electrode phase known, the model allows measuring the device's efficiency in terms of current density when an external voltage is applied.

2.4.1 Proposed geometrical designs

Each geometrical design consists of two flow channel domains separated by an ion-conducting membrane for the modeling. The thickness of the membrane was fixed throughout the study, while the depth D of the flow channels ranged from 0.5 mm to 5 mm. The circle-shaped channel geometry (**Figure 5a**) resembles the cross-sectional view of the experimental testing cell design. The other two geometrical arrangements include a box-shaped geometry (**Figure 5b**) with linear current collectors and a box-shaped geometry with the extended current collector (CC) (**Figure 5c**).

(a) Circular shaped geometry   (b) Box shaped geometry (linear current collectors)   (c) (b) Box shaped geometry (Extended current collectors)

Positive electrode   Negative electrode   Separating membrane   Current collector

D = depth of the flow channel   d = thickness of membrane
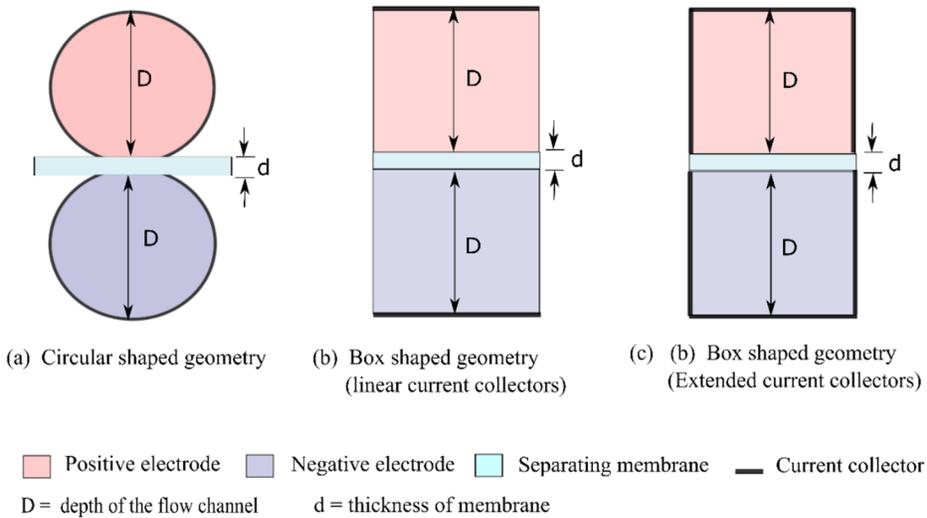
Figure 5. Geometrical design of EFC models. (a) Circular shaped geometry, (b) box-shaped geometry (linear CC), (c) box-shaped geometry (extended CC).

2.4.2 Transport of ionic species

The ionic flux (N_i) in the modeled device is described by using the Nernst-Planck equation as,

$$N_i = -D_i \nabla c_i - \frac{z_i F}{RT} D_i c_i \nabla V_2 \tag{1}$$

where c_i is the ionic concentration, V_2 is the potential in the electrolyte and D_i is the effective diffusion coefficient. The constants z_i, F, R, and T are for the ionic charge, Faraday constant, ideal gas constant, and temperature in Kelvin scale, respectively. The ionic flux is because of the diffusion and migration of ions within the model. The total flux of electrolytic ions will be,

$$N_{total} = -(D_+ \nabla c_+ + D_- \nabla c_-) - \frac{F}{RT}(z_+ D_+ c_+ + z_- D_- c_-) \nabla V_2 \tag{2}$$

2.4.3 The charge conservation equation

Ohm's law determines the electronic current in the slurry electrode phase:

$$j_1 = -\sigma \nabla V_1 \tag{3}$$

where σ is the effective electronic conductivity and V_1 is the potential in the homogenized electrode phase. The current density in the slurry electrolyte phase is,

$$j_2 = \sum_i (N_i z_i) F \tag{4}$$

The overall charge conservation under the assumption of electroneutrality states that the divergence of the system's total current density is zero.

$$\nabla \cdot j_1 + \nabla \cdot j_2 = 0 \tag{5}$$

The charge conservation equation in the electrode phase is [39],

$$\nabla \cdot j_1 = -\sigma \nabla \cdot (\nabla V_1) \tag{6}$$

The charge conservation in the electrolyte phase is [39],

$$\nabla \cdot j_2 = \nabla \cdot (\sum_i (N_i z_i) F) \tag{7}$$

$$\nabla \cdot j_2 = \nabla \cdot \sum_i \left[-\left(D_i \nabla c_i z_i F + \frac{D_i c_i z_i^2 F^2}{RT} \nabla V_2 \right) \right] \tag{8}$$

Where k is the ionic conductivity defined as,

$$k = \frac{F^2}{RT} \sum_i (D_i c_i z_i^2) = \frac{F^2}{RT} \sum_i (D_+ c_+ z_+^2 + D_- c_- z_-^2) \tag{9}$$

2.4.4 The current source in the slurry

The surface charge per unit volume, 'q' at the carbon phase, and the counter-charge per unit volume, '$-q$' from the electrolyte phase forming interface [41, 60]. So, the time derivative of this charge per unit volume is,

$$\nabla \cdot j_1 = -\frac{dq}{dt} = -Q \tag{10}$$

$$\nabla \cdot j_2 = \frac{dq}{dt} = Q \tag{11}$$

The capacitive current source Q, in the channel, determine the rate of change of the charge stored at the interface [41, 60],

$$Q = \frac{d(V_1 - V_2)}{dt} C\, a_{spec} \tag{12}$$

where a_{spec} is the specific interfacial area of carbon electrode accessible for EDL formation, and C is the EDL capacitance per unit area.

2.4.5 The mass balance and electric double layer (EDL) equation

The homogenized electrolyte phase moved through the ion-conducting membrane from one channel to another. So, the mass balance equation at any time 't' is,

$$\frac{\partial c_i}{\partial t} = -\nabla \cdot N_i + R_i \tag{13}$$

The rate of change of charge per unit volume, R_i is given by,

$$R_i = -\frac{Q}{Z_i F} \tag{14}$$

Since only negative ions are the source of EDL in the positive flow channel, so the mass balance equations are given as,

$$\frac{\partial c_+}{\partial t} = -\nabla \cdot \left(-D_+ \nabla c_+ - \frac{z_+ F}{RT} D_+ c_+ \nabla V_2 \right) \tag{15}$$

$$\frac{\partial c_-}{\partial t} = -\nabla \cdot \left(-D_- \nabla c_- - \frac{z_- F}{RT} D_- c_- \nabla V_2 \right) - \frac{Q}{Z_- F} \tag{16}$$

Similarly, in the negative flow channel, only positive ions contribute to EDL, so the mass balance equations are,

$$\frac{\partial c_+}{\partial t} = -\nabla \cdot \left(-D_+ \nabla c_+ - \frac{z_+ F}{RT} D_+ c_+ \nabla V_2 \right) - \frac{Q}{Z_+ F} \tag{17}$$

$$\frac{\partial c_-}{\partial t} = -\nabla \cdot \left(-D_- \nabla c_- - \frac{z_- F}{RT} D_- c_- \nabla V_2 \right) \tag{18}$$

As there is no homogenized electrode phase in the separating membrane to form the double layer interface, so the concentration distribution of ions is given by,

$$\frac{\partial c_+}{\partial t} = -\nabla \cdot \left(-D_+ \nabla c_+ - \frac{z_+ F}{RT} D_+ c_+ \nabla V_2 \right) \tag{19}$$

$$\frac{\partial c_-}{\partial t} = -\nabla \cdot \left(-D_- \nabla c_- - \frac{z_- F}{RT} D_- c_- \nabla V_2 \right) \tag{20}$$

The mathematical model presented is solved using the Finite element method, and Comsol Multiphysics 5.2 was used as a solver. Each geometrical configuration was divided into subdomains called mesh domains. The meshing size and element type were dependent on the size and shape of the domain. The solution to the modeled equation was calculated for each mesh element and then interpolated for the whole modeled geometry. The basic scheme of the homogenized modeling study is outlined in **flow chart 2**. The essential parameters used in the homogenized phase model are given in **Table 3**.

Table 3. Parameters used in Homogenized phase model

Para-meter	Value	Description	Reference
a_{spec}	2557 m^{-1}	The specific surface area of carbon	Estimated
C	0.22 F m^{-2}	Double layer capacitance	[61, 62]
c_0	417 mol m^{-3}	Initial concentration	Calculated
F	96400 C mol^{-1}	Faraday constant	–
R	8.32 J mol^{-1} K^{-1}	Ideal gas constant	–
T	293 K	Temperature	Assumed
V_0	0.1 V	Voltage	Assumed
z_+	1+	Charge on a positive ion	–
z_-	2−	Charge on negative ion	–
D_+	1.334x10^{-9} m^2 s^{-1}	Diffusion coefficient of positive ion (Na^+)	[63]
D_-	1.064x10^{-9} m^2 s^{-1}	Diffusion coefficient of negative ion ($SO_4{}^{2-}$)	[63]
σ	0.242 mS cm^{-1}	Electronic Conductivity	Estimated
k	111.2 mS cm^{-1}	Ionic Conductivity	Calculated
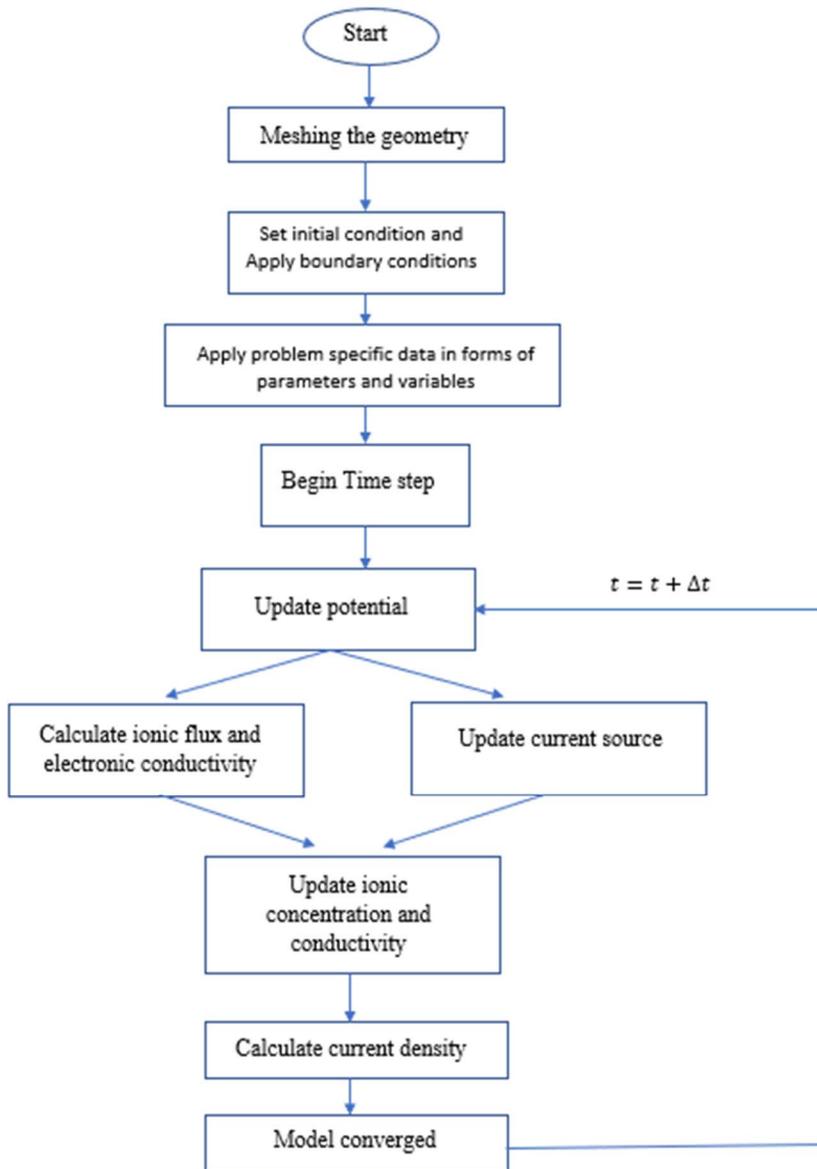
Flowchart 2 . Modeling strategy time loop in COMSOL Multiphysics.

2.5 Limitations of homogenized phase models

The homogenized phase models are classified as imposing the specific surface area capacitance and volumetric capacitance instead of predicting them [39]. The model implementation scheme consists of the high surface area electrode and the material's fixed capacitance as the current source. The active material of flowable slurry electrodes themselves has inadequate electrical conductivities. Therefore, the carbon/binder phase distribution in the pore space between the active material particles is essential for improving the electronic transport path from the current collector to the active material phase [64]. The absence of microstructures in the homogenized model can not explain and predict the contribution of side redox reactions related to the electrode-electrolyte interactions. If part of the active material is not electronically connected, it does not contribute to the storage capacity of the material. Integrating mathematical homogenization modeling theory to stochastic modeling provides an effective tool for deriving models that accurately anticipate various macroscopic behavior and the electrochemical properties of flowable slurry electrode charging to optimize and manufacture high-performance energy storage systems. A summary of the integrated homogenized and stochastic modeling advantages is illustrated in **Figure 6**.
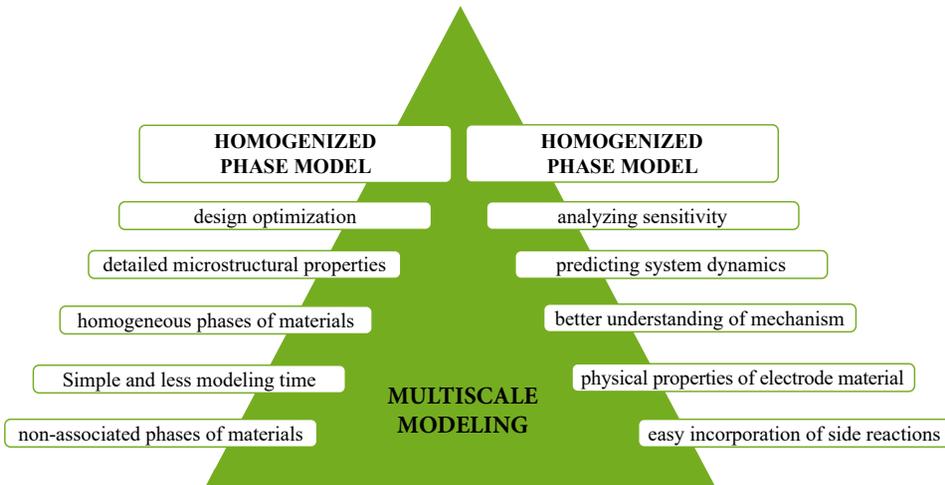
Figure 6. Mutual benefits of homogenized phase model and particle-based model in multiscale modeling.

## 2.6 Particle-based Stochastic model

For the growing interest in developing more efficient and accurate tools to aid experimental scientists in designing energy storage technologies such as EFC, stochastic modeling is capable of integrating the microscopic mechanisms which enables predictability of the systems, chemical and structural properties, and the

influence of molecular fluctuations on the systems [65]. The modeling approach developed here is used to track the single-phase carbon particles in a spherical shape while interacting together in a dense phase.

The prepared and electrochemically tested FEs contain approximately 1.8×10^{17} identical rigid carbon particles in 1 cm^3. The concept of superparticles (SP) representing many real particles interacting at an overlapping interaction distance was used to make simulation efficient. So, the building block of the model is not made of single carbon particles but rather of collective clouds of them. Each SP (as a computational particle) represents a group of particles that can be visualized as a small piece of phase space. The SPs were immersed in the background fluid, water with standard viscosity and density. In this case, the trajectories of positions and velocities of the SPs center of mass constitute a sufficient characterization of the system's evolution in phase space [66]. In the model, rescaling the number of real carbon particles to the number of SPs was viable because the Lorentz force's acceleration depends only on the charge-to-mass ratio so that each SP follows the same trajectory path as a real carbon particle [67].

The advantage of such a modeling approach is its capacity to include arbitrary side reactions or interactive forces in the modeling system. **Figure 7** shows the main idea depicting the lumping of several real particles into a distribution of SPs. The model is valid for the diameter of SP smaller than the flow channel width and several orders more significant than the size of carbon particles.
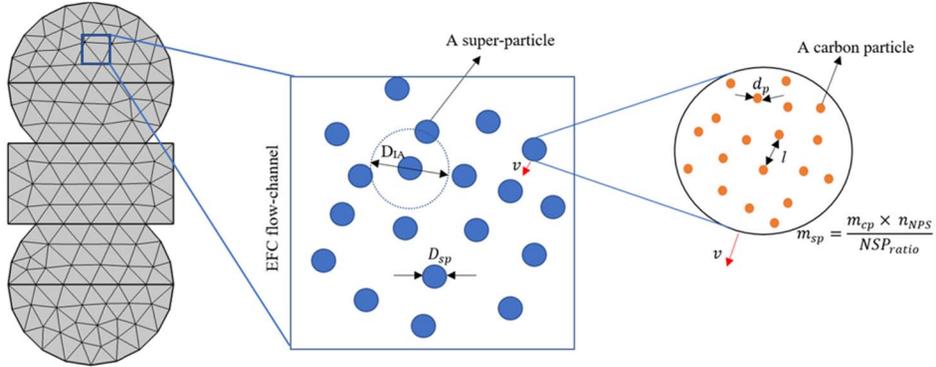
Figure 7. Schematics of carbon particles and super-particles in a meshed EFC cell for parameters representation (Not to the scale).

2.6.1 Governing equations

The flow channel domain was divided into coarse mesh elements. The position of SP released in the flow channel at a time t is given by $q_i(q_{ix}, q_{iy}, q_{iz})$ and the velocity at q_i is given as $v_i(v_{ix}, v_{iy}, v_{iz})$. The carbon particle or SP carries zero physical charges when released in the flow channel. Each SP velocity initialized in the flow channel following Maxwell's velocity distribution, given by

$$f(v_i) = \sqrt{\frac{m_{SP}}{2\pi k_B T_0}} \exp\left(\frac{-m_{SP} v_i^2}{2 k_B T_0}\right) \tag{21}$$

Here k_B is the Boltzmann constant, $T_0 = 273$ K is the temperature in Kelvins and m_{sp} is the mass of the SP. The only interaction incorporated is hydrodynamic in nature, i.e., it arises from the superposition of the velocity fields of the various particles. This field induces a force field that in turn influences particle movement. All other possible interactions (e.g., van der Waals dispersion forces, particle interaction through gravity, or resulting from positive and/or negative charges) are assumed to be either nonexistent or negligible in this situation being analyzed here [66]. When each SP moves, it conserves the linear momentum as:

$$F_t = \frac{d(m_{SP} v_i)}{dt} \tag{22}$$

The variable F_t is the total force acting on the SPs. The stochastic nature of the model also allows the facile addition of external fields dependent forces such as drag force, dielectrophoretic force, and Brownian force, among others, depending on the requirement. For this study case, the Brownian movement in microscale is negligible [68, 69], the drag and dielectrophoretic forces for spherical particles in an infinite medium without any neighboring particle are of the order of 10^{-16} which is considered ineffective for such systems [69, 70]. The total mass of an SP, m_{SP} is dependent on how much is the mass of a single carbon particle, m_c and the total number of carbon particles in a SP, n_{NPS},

$$m_{SP} = \frac{m_c \, n_{NPS}}{NSP_{ratio}} \tag{23}$$

where NSP_{ratio} is the constant ratio defined on the base of SP needed in the system, N_{sp} over the number of SP actually used in the model of a flow channel. The size of SP itself is influenced by the physical properties of carbon particles and the Volume V of the electrode flowing channel. If D_{sp} is the diameter and V_{sp} is the volume of the SP, then the total number of SP needed in the Flow channel is given as,

$$N_{sp} = \frac{V \, D_{sp}}{L \, V_{sp}} \tag{24}$$

here L is the length of the flow channel. Theoretically, the number of carbon particles in a superparticle can be estimated by using the V_{sp} and volume of a single carbon particle, v_p.

$$n_{NPS} = \frac{V_{sp}}{v_p} \tag{25}$$

Each SP, carrying thousands of carbon particles in the flow channel, obtains surface charge while scattering from the current collector (CC) [71]. The particles–CC boundary interaction forces enough momentum exchange between neutral SPs and CC to move SPs away from the CC. Thus, the hydrodynamic force from eq (22) is enough for the SP to scatter it back in the flow channel after charging at the CC boundary.

In the positive flow channel, the neutral SPs scatter from the CC boundary and obtain random charge, β_{Na} representing the sodium ion (Na^{+1}) adsorption on the surface of carbon particles. In the negative flow channel, carbon particle gains the random charge, β_{SO_4} representing sulfate ion ($SO_4{}^{2-}$) adsorption. The SP charging scheme at the boundary and charge distribution within the interaction range are given in **Flow chart 3**.

$Z_p = Charge\ on\ a\ superparticle$

No

$Z_p = 0$

Yes

$Z_p = \beta_{Na} \cdot \Delta q$ (Positive channel)

$Z_p = \beta_{so4} \cdot \Delta q$ (Negative channel)

$Z_p > 0$

$Z_p < 0$

Yes

$Z_p = Z_p + \beta_{Na} \cdot \Delta q$ (Positive channel)

$Z_p = Z_p - \beta_{so4} \cdot \Delta q$ (Negative channel)

While $1 \leq \Delta q \leq 10$ (positive Channel)

While $-2 \geq \Delta q \geq -5$ (Negative channel)
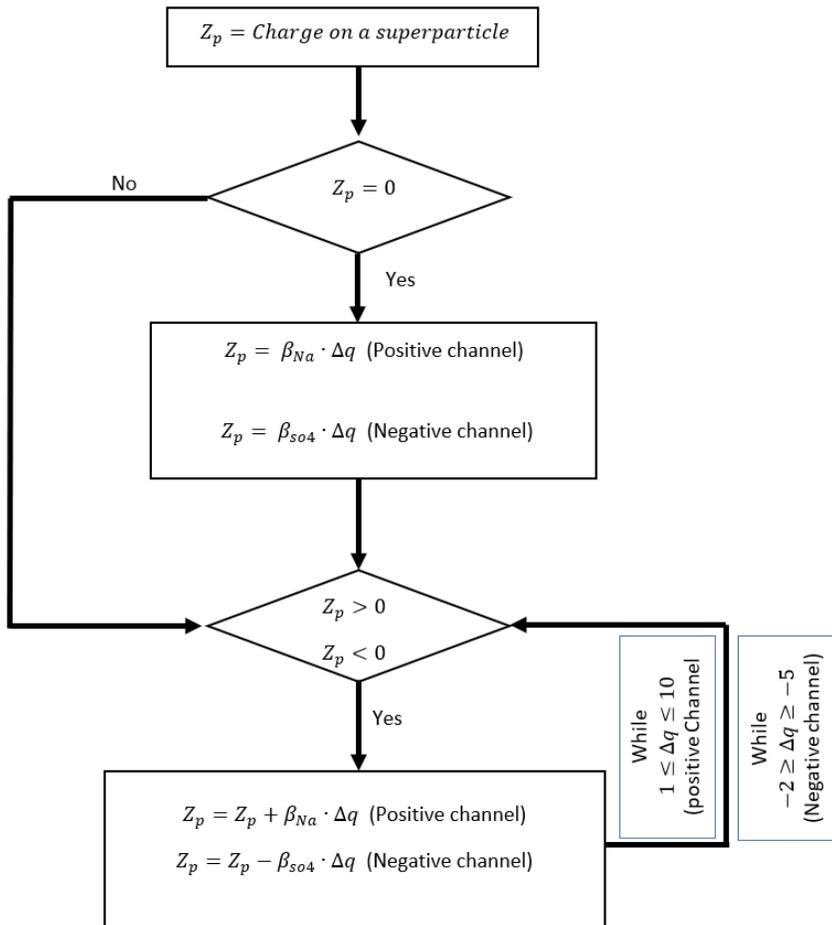
Flow chart 3. Initialization of SP charge distribution based on the defined particle model.

The Z_p is the charge of the SP, and Δq is the charge difference (before and after) of the SP. Since the SPs number in the flow channel is adjustable and interact randomly with other SPs while drifting through the flow channels. The charge transfer between SPs is also considered arbitrary. If the average number of positive ions (Na$^+$) for a carbon particle is β_{Na}, then the number of negative ions (SO$_4{}^{2-}$) for the carbon particle is $\beta_{SO_4} = 2 \times \beta_{Na}$ (charge neutrality). Within interaction diameter range D_{IA}, SP redistributes its charge to the neighboring SPs while conserving the total charge [72]. This recurring charge transfer overtime is calculated by a state variable u, given as

$$f(u, u_t, u_{tt}, t) = 0 \tag{26}$$

with initial conditions $u(t_0) = u_0$ and $u_t(t_0) = u_{to}$

The subscript t is fr representing the time derivative of the respective variable. The variable is the function of the total charge Q as an average of both flow channel cross-sectional dimensions:

$$Q = \frac{1}{2}\left(Q_{Na} + (-Q_{SO4})\right) \tag{27}$$

where Q_{Na} is the accumulated charge in the positive channel of the geometry and Q_{SO4} is the accumulated charge in the negative channel of the geometry. The total amount of charge along the length L of the flow channel is estimated by

$$Q_t = \frac{Q}{L} \times D_{sp} \times e \tag{28}$$

where L here is the z-dimension length of the flow channel and e is the constant electronic charge. While preparing and implementing the model following assumptions were made:

1. Mass, momentum, and charge are rigorously conserved.

2. The carbon particles and super-particles have a constant size and mass.

3. Each particle scatters from the CC boundary and gains a random physical surface charge.

4. The interactive forces between the computational particles, e.g., Dielectro-phoretic and Brownian forces, are negligible [68, 70].

2.6.2 Model implementation

The particle-based stochastic model is implemented for three different geo-metrical designs shown in **Figure 5(a–c).** The model was implemented using COMSOL Multiphysics 5.5. **Flow chart 4** shows the schematic loop diagram of

the numerical solution. This loop is carried through all the particles individually in each time increment. The loop also goes through all the contact super-particles within the interaction range to calculate the total charge. The important parameters for particle-based model are given in **Table 4.**

Table 4. Parameters for particle-based model

Geometry design parameters			
Parameter	**Symbol**	**Value**	**Reference**
Diameter of a flow channel	D_{fc}	5 mm	[46, 48]
Length of a flow channel	L	120 mm	[46]
Volume of a flow channel	V	2.3562×10^{-6} m^3	–
Carbon particles parameters			
Diameter of carbon particle	d_p	50 nm	[46, 48]
Volume of carbon particle	V_p	6.545×10^{-23} m^3	Calculated
Number of carbon particles in 1g	n_c	6×10^{18}	Calculated
Flow velocity of the slurry	u_0	1.69 mm/s	[48]
Total no. of carbon particles in the slurry		1.8×10^{14}/mm^3	Calculated [46]
Total no. of electrolytic ions in the slurry		1.8066×10^{14}/mm^3	Calculated [46, 48]
Mass of single carbon particle	m_{cp}	1.67×10^{-19} g	Calculated
Number of Na ions per carbon particle	β_{Na}	1	estimation required
SP parameters			
Diameter of an SP	D_{sp}	100 μm	estimation required
Volume of an SP	V_{sp}	5.236×10^{-13} m^3	–
Average number of carbon particles in an SP	n_{NPS}	9.4248×10^{10}	Calculated
Number of SPs needed	$needed_{NSP}$	2.0281×10^5	Calculated
Number of carbon particles in an SP	NPS	1.885×10^{11}	–
Number of carbon particles should be in an SP	NC_{box}	7.0686×10^{14}	–
Total volume of SPs	V_{SP}	3.927×10^{-9} m^3	–
Interaction diameter of SPs	D_{IA}	D_{SP}	–
SPs actually used in each channel	$actual_{NSP}$	2000	estimation required
Ratio of needed to actual SPs	NSP_{ratio}	$\dfrac{needed_{NSP}}{actual_{NSP}}$	–
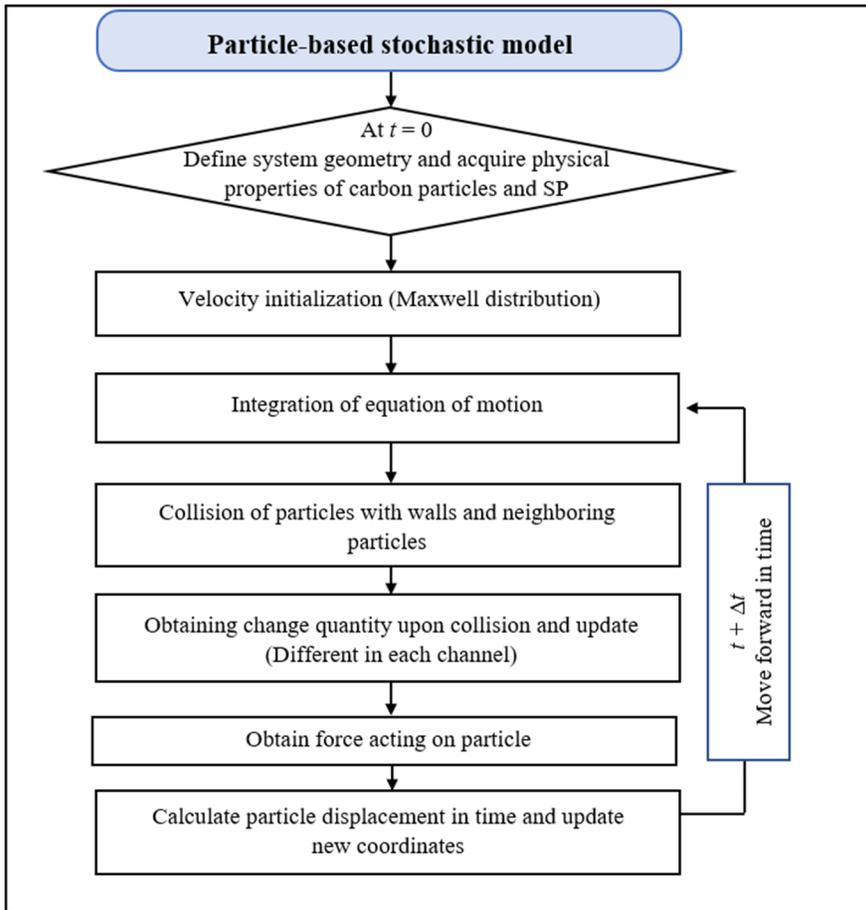
Flow chart 4. Loop diagram of the numerical solution process

2.7 Parametrization of an EFC model

One major challenge is the parametrization of the computational models. Model calibration strategy is to estimate the values of the essential parameters and there-after change the parameters with their estimated value to conclude the sensitivity relation with the final outcome of the model. The mathematical parametrization problem is solved when a real-valued function is either maximized or minimized relative to a given set of feasible alternatives. It is reliable to determine the values of the parameters that provide simulated data that best matches the measured data. Once the basic models are implemented, the parametrization is performed for input parameters by minimizing the objective function (OF) [73, 74]. The OF is the sum-of-squared differences between the model outputs and the experimentally measured values for each cycle i,

$$OF = min_{\theta i} \sum_{j=1}^{n_i} \left[y_i(t_i) - y_{model,i}(t_i; \theta_i) \right]^2 \qquad (29)$$

where $y_i(t_i)$ is the experimentally measured output in time t_i for cycle i, $y_{model,i}(t_i; \theta_i)$ is the model computed output at a time t_i for cycle i for selected model parameters θ_i (the parameters estimated from the experimental data), and n_i is the number of time points cycle i.

3. RESULTS AND DISCUSSIONS

3.1 Basic properties of the electrode slurry

All the electrochemical measurements of the slurry electrodes were performed at room temperature. The electrochemical impedance spectroscopy (EIS), cyclic voltammetry (CV), and the current measurement at a constant voltage in a testing cell device were carried out using BioLogic Potentiostat (Publication **I**).
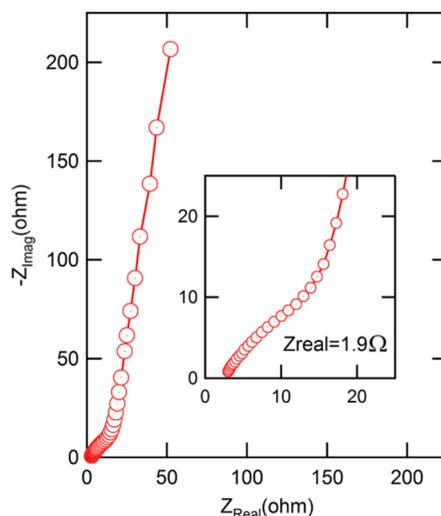
Figure 8. Nyquist plot for the tested flow electrode (FE) measured at 0V cell potential using 5mVrms.

Electrochemical impedance spectroscopy (EIS) measures the impedance of the flow cell. EIS measurements were performed using a static flow-cell configuration at 0 V. The Nyquist plot obtained by the impedance spectroscopy method is shown in **Figure 8**. Slurry electrodes exhibited nearly vertical lines in the slow frequency region, indicating primarily capacitive behavior. The inset provides more detailed high and mid-range frequency information and estimates the equivalent series resistance (1.9 Ω).
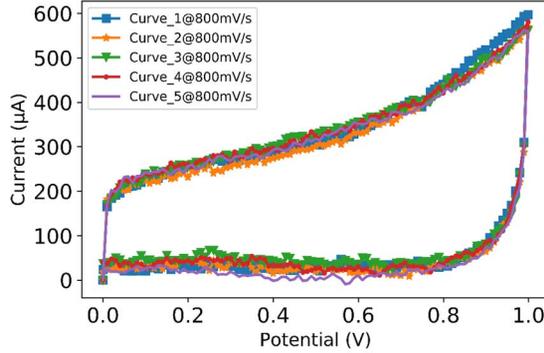
Figure 9. Potentiostatic charging of the carbon slurry at the scan rate of 800 mV/s.

The cyclic voltammetry (CV) scan was performed within the potential range of 0–1 V and at the scan rate of 800 mV/s, shown in **Figure 9**. This scan rate was chosen because of the low carbon concentration in the slurry electrode. The measurement was performed with a two-electrode system. The capacitive nature of the carbon electrode causes a sudden increase in the slope as voltage goes from 0–0.2 V. The gradual increase of potential from 0.2–1 V shows the fast-growing faradic current in the slurry charging. To minimize the faradic current contribution, current and voltage efficiencies were obtained in voltage and current control mode (**Figure 10**). The method utilizes a constant applied voltage, and subsequent current response is used to measure the electronic conductivity. The electronic resistance can be calculated from Ohms law.

$$R_e = \frac{\Delta V}{\Delta I} = \frac{V_f - V_i}{I_f - I_i} \tag{30}$$

The electronic resistance goes from 6.9 kΩ to 5 kΩ at the constant current of 50 µA (**Figure 10 inset**).
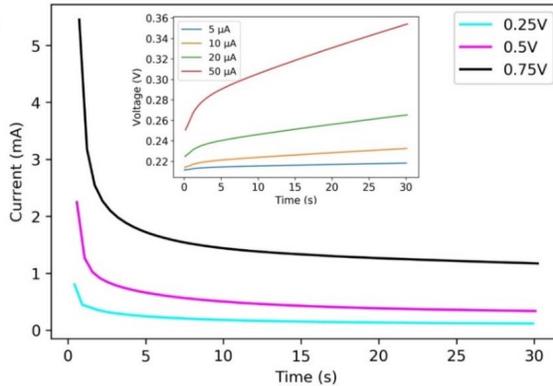
Figure 10. Potentiostatic measurement at constant voltage of 0.25 V, 0.5 V and 0.75 V. Inset, at constant current of 5 µA, 10 µA, 20 µA, and 50 µA

3.2 Carbon slurry as homogenized media

3.2.1 Calibration of homogenized phase models

The calibration of the homogenized phase model for the EFC is used to estimate the properties of carbon particles – specific surface area, a_{spec} and the electronic conductivity, σ. All the parameters defined in the homogenized modeling method are given in **Table 3**. Cyclic voltammetry current scans are used as the real measured values $y_i(t_i)$, for minimizing the OF from eq(29). Experimental data is used as input of the homogenous modeling parameters, optimized the surface area of carbon with electronic conductivity.

The parameter estimation problem was solved using the circular-shaped CC geometry with each channel 5 mm wide. The electrical current computed in the model is $y_{model,i}(t_i; \theta_i)$ depending on the control parameters, θ_i. The problem is solved using a gradient-free algorithm BOBYQA (Bound optimization by quadratic approximation) [75]. The basic notion of the method is to choose an initial value and improve it computationally at the end of each iteration. The accuracy of the finely-tuned control variable depends on the optimality tolerance (OT), which by default, is 0.01. The final numerical values obtained for a_{spec} stabilized at 2557 m^{-1}, and for σ at 0.242 mS/cm. The non-faradic current due to EDL formation is observed at low voltages. At a scan rate of 800 mV/s, 0 to 0.2 V corresponds to 0 s–0.25 s in the time scale used to compare the experiment. For the double-axis graph in **Figure 11**, the current vs. voltage (0–0.2 V) is from experiments, and current vs. time is for the temporal evolution of current in simulations. The result shows a good agreement between the current collected in experiments and simulations (Publication **II**).
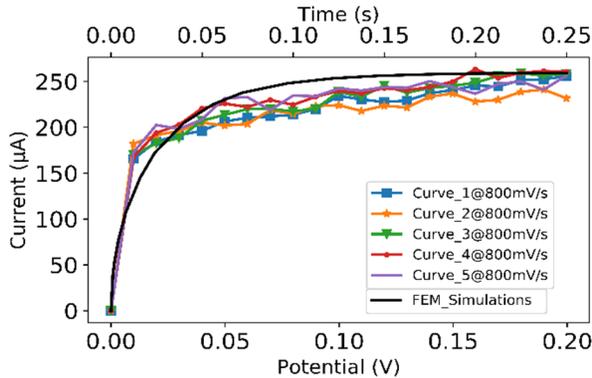

Figure 11. FEM simulation for Flow capacitor model in comparison with the experimentally measured current.

### 3.2.2 Current density in circular shaped current collectors

The current density distribution in the carbon slurry phase of the model is shown for selected time frames in **Figure 12**. Since the non-faradic current was observed only in early time, the 1 ms, 130 ms, and 250 ms were highlighted here. The voltage V_1 polarizes the stationary carbon surface area in the flow channels so that the electronic current transferred from CC to the homogenized carbon phase is given by eq (3). The carbon phase comparatively close to the CCs is at a higher potential and decreases rapidly with distance. The sodium ions are electrostatically attracted to the negatively charged carbon surface, while sulfate ions are drawn to the positively charged carbon in the respective flow channel. The flux of those ions is due to the migration and diffusion phenomena, eq (1) and (2). The model's freely moving sodium and sulfate ions induced the diffusion potential V_2, and their conductivity due to migration and diffusion is given by eq (9). The change of the V_1 and V_2 directly affects the current source in the flow channels, given by eq (10) and (11). For the modeled device, the ionic conductivity is 111.2 mS/ cm, which is much higher than the electronic conductivity, causing the maximum density of charging current near CCs. The carbon phase away from the CC is not activated by V_1 and instantly reduces the current density distribution leading to carbon underutilization. Li et al. also reported a similar conductivity difference for linearly flowing slurry [60, 76]. The carbon phase near the CCs allows the transport of counter-ions to the respective flow channel for electric double layer adsorption given by eq (15)–(20). The concentration of sodium ions becomes higher around the negative CC, while sulfate ions become excessive around the positive CC. The CCs also form the sharp corner with the ion-conducting membrane and act as a localization of the applied voltage. Such localized voltage was responsible for the high current density at the sharp corner of the flow channel and membrane [55, 77].
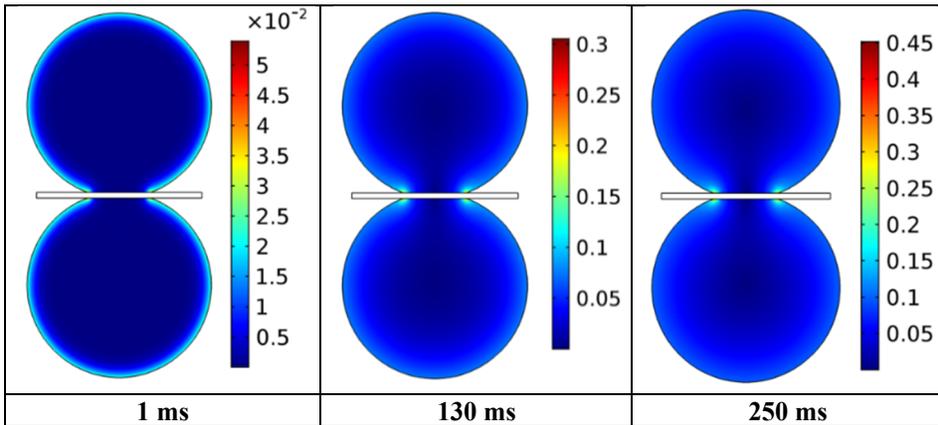
Figure 12. The current density in the homogenized carbon phase (A/m^2) at 1 ms, 130 ms, and 250 ms.

3.2.3 Flow channel design

For the purpose of effectively designing the EFC, the size of the modeled geometry was changed from 0.5 mm to 5 mm wide flow channel. Depending on the size of the circular flow channel, the area of the current collector directly in contact with the carbon phase changes from 188.4 mm^2 to 1884 mm^2. The scale-up of the flow channel depth (from 0.5 mm to 5 mm) increases the current because of proper contact between the CC and the carbon surface area (approx. ten times) and the resistance drop [78]. **Figure 13 (a,b)** demonstrates the maximum current in the carbon phase for the channel depth, ranging from 0.25 mm to 5 mm at 250 ms of time. The large channel depth also affects the diffusion distance for the electrolytic ions (sodium and sulfate) so that a much longer time is needed to arrive at the active sites of the carbon phase (Publication **II**). Thus, the larger the flow channel size, the more time the device needs to achieve charge saturation. To enhance the carbon utilization in the flow channel, mediate size channels should be used without compromising the carbon phase charging.
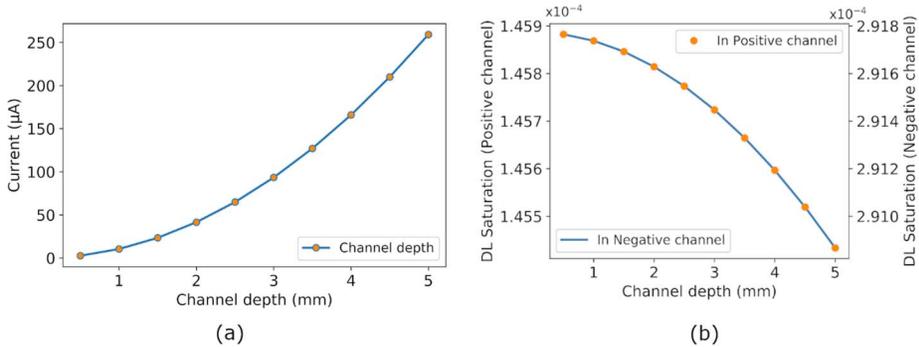
Figure 13. (a) Charging current as a function of channel depth in circular symmetric geometry. (b) EDL saturation against the size of the flow channel.

3.2.4 Current density in box-shaped geometry

The current density distribution for the homogenized carbon phase in the box-shaped geometry for two different configurations is given in **Figure 14(a,b)** below. The 5 mm long, linear CCs in the box-shaped geometry show the inactivity of carbon phase charging near the membrane area. The high current density was observed near the CCs, and the carbon phase was readily available for accommodating the electrolytic ions. On the other hand, the extended CCs experience the sharp corner localization of charge similar to the circular geometry design; hence the carbon phase underutilization increase around the sharp corners of the box geometry. The uniform charging behavior near the linear CC boundary proves that avoiding sharp corners between CC and membrane improved carbon charging in the flow channel. The surface area of CCs in box geometry with extended CCs for a 5 mm wide flow channel is about 1800 mm^2 (quite close for

the circular geometry channel, 1884 mm^2). However, the current density experiences a huge drop from 0.45 A/m^2 to 0.25 A/m^2 (Publication **II**).
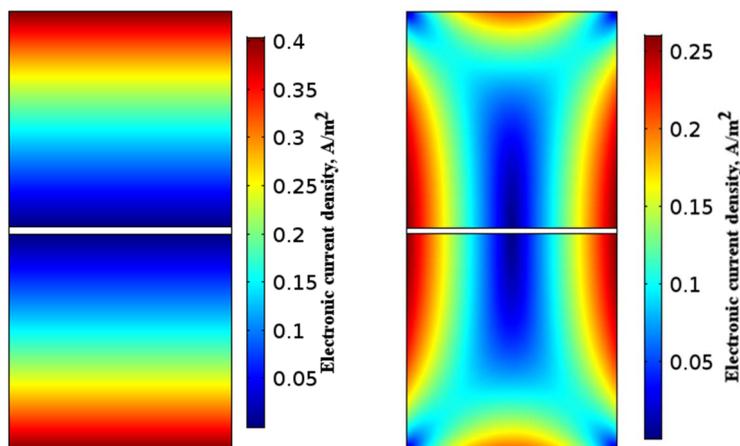
Figure 14. Current density distribution for Box-shaped geometry (a) with linear CCs, (b) with extended CCs.

3.2.5 Asymmetric geometry design

The asymmetric geometry model differs in the flow channels size while keeping the thickness of the separating membrane at 150 μm (Publication **II**). In a Box geometry with linear CCs, the size of the positive flow channel was kept half of the size of the negative flow channel. If the negative flow channel was 5mm (Distance between membrane and CC), the positive channel was kept 2.5 mm wide. When the size of the positive channel was halved w.r.t negative channel, the ionic density in the positive channel doubled along with comparatively shorter diffusion lengths. When the negative channel depth was 5 mm, and the positive channel was 2.5 mm deep, the ions rushed to the counter-charged carbon for adsorption. Initially, the DL saturation was observed to be exactly half, just like the size of the channel, but soon after a few ms of time, the equilibrium started to set in, shown in **Figure 15(a,b)**. The DL saturation in the positive channel starts to increase at the same rate with a decrease in the DL saturation in the negative channel until an equilibrium is achieved [79, 80]. Smaller the size of the channel, less time is needed for the system to stabilize.
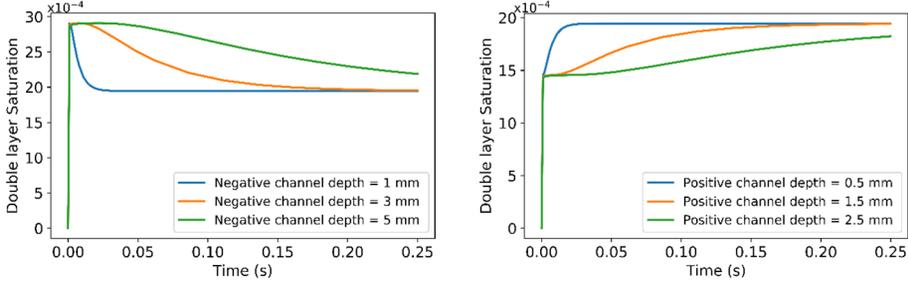
Figure 15. Box asymmetric geometry with linear CCs: Evolution of DL saturation of carbon (a) In positive flow channel, (b) In negative flow channel.

3.3 Carbon slurry by discrete particle-based model

In addition to the parameter estimation, the parametric study aided quantify the influence of the no. of SPs used in the flow channel, $actual_{NSP}$ and the interaction diameter, D_{IA} on the charging of carbon electrodes in the EFC circular-shaped geometry. The variation in positive ions per carbon particle, β_{Na}, was calculated as a function of the $actual_{NSP}$ and the interaction diameter.

3.3.1 Parameter estimation of the particle-based stochastic model

The parameter estimation of the particle-based stochastic model is performed by using the similar minimization of objective function method from section 2.7. However, the accumulated charge is now counted instead of the electrical current. The EFC charging current at a constant voltage is used to provide a stable real value with reference to which the particle model results are optimized. Since the particle-based model output is measured in charging the carbon SPs, the experimentally measured current is integrated to obtain the charge stored in the carbon FEs. This integrated charge quantity is used as the experimental real value, $y_i(t_i)$ and $y_{model,i}(t_i; \theta_i)$ as the model computed charge in eq (28). Since the charge is an integral quantity, it is thus significantly less sensitive to numerical noise than current. This becomes notably important in this approach due to the stochastic nature of the implemented particle-based approach. The design parameters θ_i for the particle-based model are SP size in terms of D_{sp} and mass m_{sp}, the actual number of SPs $actual_{NSP}$ and the average positive ions per carbon particle β_{Na}. The scales and upper / lower bounds for control parameters are given in **Table 5.**

Table 5. Parameters used in optimization with their upper and lower bounds.

Parameter	Initial value	Scale	Lower bound	Upper bound	Exact
Diameter of SP, D_{sp} (µm)	100	1	80	120	99.3
Mass of SP, m_{SP} (kg)	8.3943×10^{-13}	1	8.3943×10^{-14}	8.3943×10^{-12}	8.3943×10^{-14}
Actual no. of SPs used, $actual_{NSP}$	2000	10	4020	4100	4031
No. of ions (Na^{1+}) per carbon particle, β_{Na}	1	10	0.14931	1.8618	0.69154

In the parameter estimation study, the total charge obtained by integrating potentiostatic EFC current under the constant voltages of 0.75 V was used as experimentally measured results. The numerically estimated charge was obtained from eq (29). The calibration of the particle-based model is shown in **Figure 16**. The error analysis is done based on a comparison of the experimental measurements and the model's predictions – a comparison of them showed excellent agreement (Publication **III**). The maximum difference of the charge obtained by model and experiment was 1.406×10^{-6} C. The error measure ΔC is given as,

$$\Delta C = \frac{(\text{simulation point} - \text{experimental point})}{(\text{simulation point} + \text{experimental point})/2} \times 100\ \% = 8.3\ \% \tag{31}$$
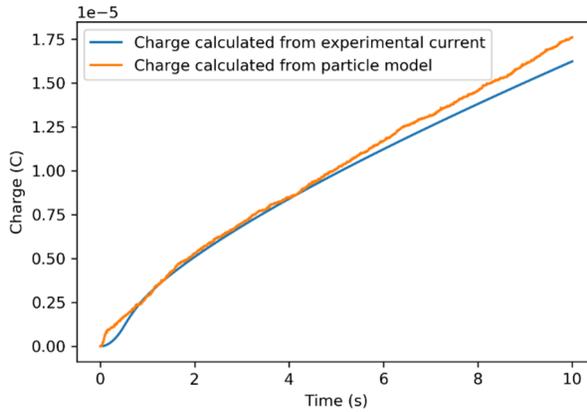
Figure 16. Experimental vs. numerical charge estimated data for 0.75 V potentiostatic charge.

3.3.2 Sensitivity analysis of model parameters

Influence of superparticles (SPs) number

According to the underlying mesh, SPs are released on boundaries and domains uniformly, as defined by a grid. Usually, the particle simulation suffers from too many particles in the total system [81]. The size of SP can only be increased to a

limit; a higher number of SPs in a channel can render the computation slow and costly. Increasing the size of SP will increase their weight and slow them down in the system. On the other hand, controlling the SPs number can potentially balance the computation cost and speed [81, 82]. The model calibration estimates flow channel contained 4031 SPs, and for each carbon particle, there are 0.69154 positive ions for double layer charging of carbon particles (Publication **III**). Increasing the number of SPs would effectively decrease their mass, facilitating efficient diffusion in the channel. Hence, more trajectory intersections could facilitate the charging of electrodes particles over time. The model anticipated the better charging of the particles when the number of SPs was doubled. Changes in β_{Na} against varying $actual_{NSP}$ at the constant voltages of 0.75 V, 0.5 V, and 0.25 V shown in **Figure 17**. This change in positive ion availability was much more prominent at higher voltages, supporting better carbon electrode utilization. The change in β_{Na} showed an almost linear relationship for a fewer number of SPs. The change in β_{Na} was observed to be much more prominent at the higher voltages when SPs in the channels were above and below the estimated value. The model suggests that the low voltages are suitable for electric double-layer charging.
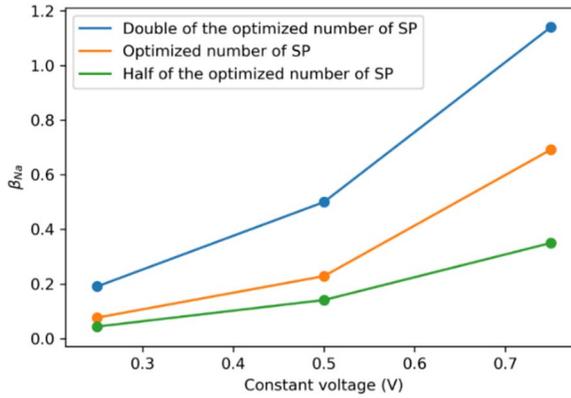
Figure 17. Changes in β_{Na} against varying $actual_{NSP}$ at the constant voltages of 0.75 V, 0.5 V, and 0.25 V.

Interaction diameter of the SP

The interaction diameter, D_{IA} represents a small area in the channel where the SPs interact and redistribute the surface charge homogenously. The SPs obey the law of conservation, for example, the mass and charge when leaving the interaction diameter range. The interactions between particles are essential for the charging process in the semi-solid electrode system.

The calibration of the model was accomplished by using the interaction diameter equal to the size of an SP. The effect of interaction diameter on the positive charge per carbon particle, β_{Na} is shown in **Figure 18**. Keeping the superparticle size fixed at the estimated value of $D_{Sp} = 99.3$ μm the β_{Na} is increased because of the reduced scattering possibilities for other SPs (Publication **III**). The

numerical analysis showed that the relation between SPs is asymptotic when the interaction distance increases. For the interaction range comparable to the size of SP, the interaction was most productive for the uniform charging of the semi-solid electrode in the flow channel [83]. The change in β_{Na} at the lower voltages was practically negligible, yielding poor operating conditions. The utilization of carbon and charging productivity expected to improve at the voltages higher than 0.25 V, resulting in more efficient charging of slurry electrodes. Numerical calculations were performed using the experimental results of EFC charging at a constant voltage of 0.75 V, 0.5 V, and 0.25 V.
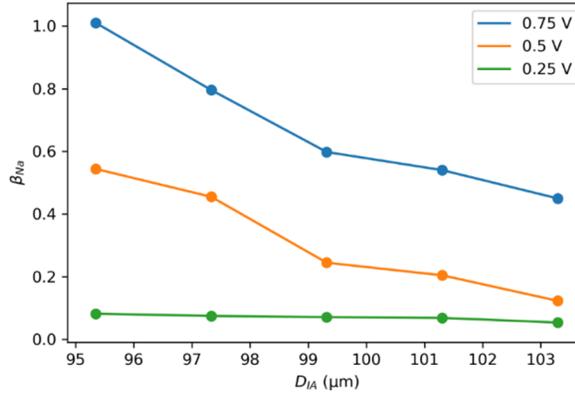
Figure 18. Effect of the interaction diameter on the average charge number, β_{Na} when $D_{sp} = 99.319$ μm.

Effect of SP size

The suitable size of an SP is limited to the size of actual particles and the size of the simulated device dimensions. Increasing the SP size can smear out the fundamental carbon particle properties. Too small SP size could also influence the interpolation of the total charge in the flow channels [84, 85]. Increasing the SPs size also increases the mass because of the number of carbon particles in an SP, represented by eq (23) and (24). Despite the effective interaction range, this extra weight slows the SP movement in the flow channel, affects SP trajectories, and limits charge distribution (Publication **III**). However, variation in β_{Na} for when decreasing the SP size by 2 % and 4 % was considerably more prominent, hence improving the availability of carbon particle charging, shown in **Figure 19**. The β_{Na} drops down fast and shows very little changes when the SP size is increased by fixed proportion anticipating the difficulty of charging carbon particles. The numerical analysis was performed using the experimental reference data of EFC charging at a constant voltage of 0.5 V.
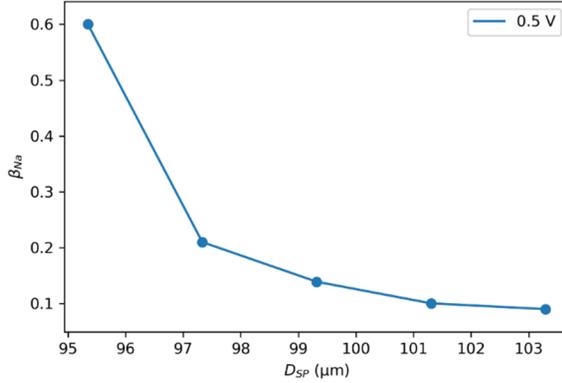
Figure 19. β_{Na} as a function of SP size with $D_{IA} = D_{SP}$.

3.3.3 Comparison between three different geometries

Using estimated parameters from **Table 5**, the circular EFC geometry is the most favorable geometrical design for charging carbon-based flowable slurry. This particle-based model was used to test the SP charging in three different EFC architecture designs (discussed in section 2.4.1). **Figure 20** shows the plot of the total charge in the EFC model for the three geometries. The charging of the carbon particle was prominent near the current collectors of the device. The model also predicted the inactivity of charging in the centers of the flow channels [46, 48] in terms of uncharged SPs when moving away from the current-collector (CC) boundary. **Figure 21** shows the charging behavior in the flow channel for three geometries. The charging process was more prominent near the CCs, leaving the central regions uncharged (Publication **III**). The carbon superparticles in the circular channel exhibited maximum charging and carbon utilization, as shown in **Figure 21 (a)–(d)**. The charge diffusion is predicted to be less effective for the carbon in the box-shaped geometry with a linear and extended CC, hence slowing the charging rate, as shown in **Figure 21 (e)–(l).**
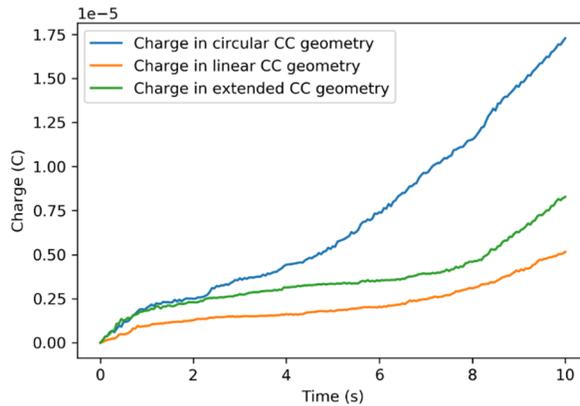
Figure 20. Total charge in three geometrical designs when optimized values of modeling parameters at the constant voltage of 0.75 V.

Time (s)	5	10	20	30
Circular CC geometry				
	(a)	(b)	(c)	(d)
Linear CC geometry				
	(e)	(f)	(g)	(h)
Extended CC geometry				
	(i)	(j)	(k)	(l)

The color bar represents the charge distribution in the flow channel as the charging of the carbon slurry electrodes progresses.
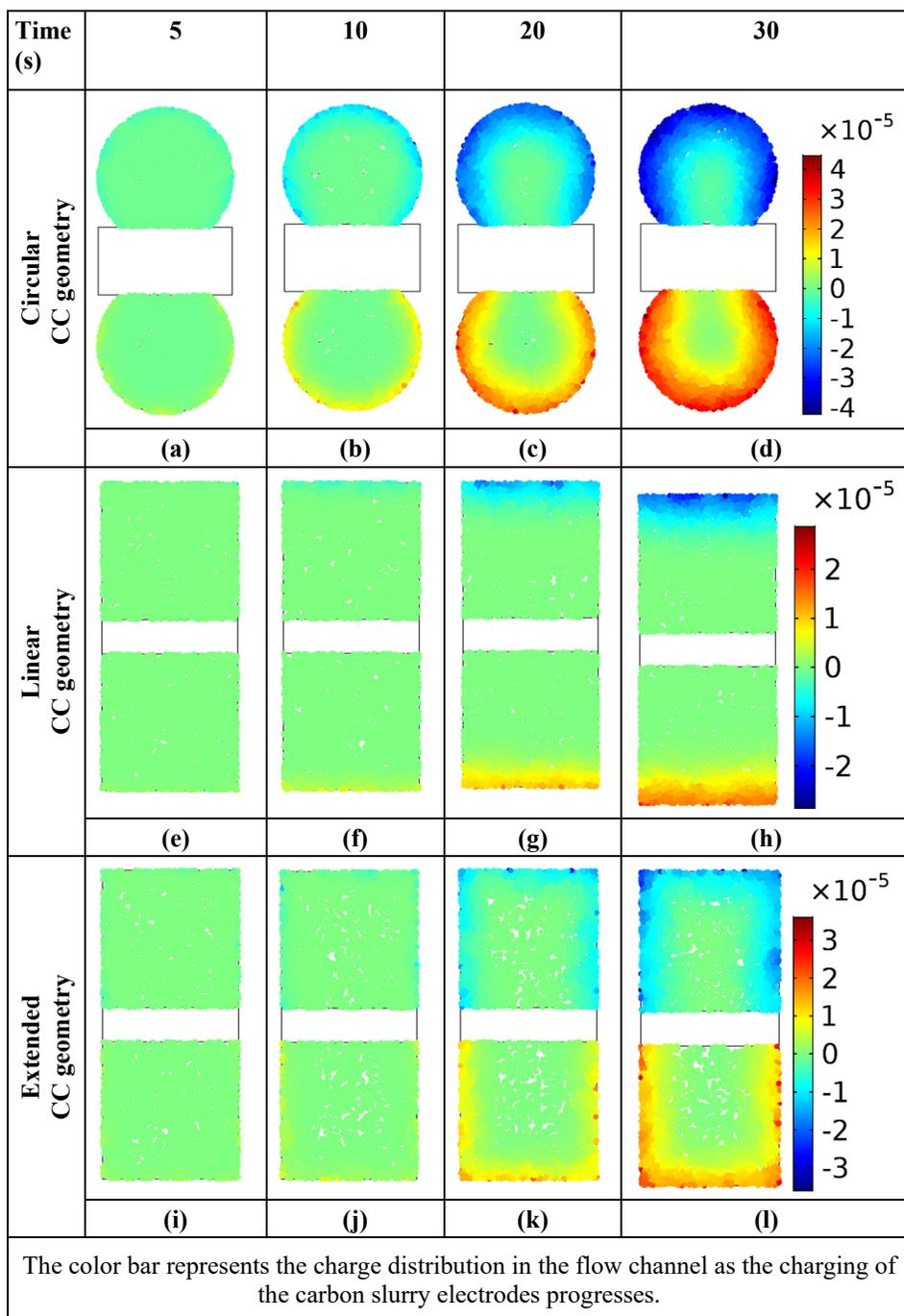
Figure 21. Charging of carbon slurry electrodes in the flow channel after 5, 10, 20, and 30 s for three geometrical arrangements, when model optimized at the constant voltage of 0.75 V. For circular-shaped flow channel see (a–d), for box-shaped channel geometry with linear CC see (e–h), and box-shaped channel geometry with extended CC see (i–l).

49

4. CONCLUSIONS

"Development and Optimization of Electrochemical Flow Capacitor"

An electrochemical flow capacitor (EFC) is a conceptual approach to meet large-scale electricity storage. This device is similar in operation to a supercapacitor but uses a concentrated solution of carbon micro and nanoparticles and an electrolyte instead of solid electrodes. It typically flows in channels with a diameter of a few millimeters, the wall of which is a flow collector and through which the liquid electrode material is pumped. A porous ion-conducting membrane separates the electrodes. Using carbon-based liquid electrodes in the device under development will allow the technology to be significantly scaled up and integrated into existing electricity grids and used effectively to support renewable energy production.

The central goal of the work presented is to understand the fundamental properties of EFC technology. As a result, EFC laboratory tests and computer simulations have been performed to design and optimize the device architecture. In the field of simulations, both existing electrochemical models have been adapted for EFC modeling, and a new stochastic model based on Monte-Carlo principles has been developed. Both implemented and developed models were thoroughly calibrated and validated against laboratory experiments and used to understand the flow electrode charging process in three fundamental EFC device designs.

Models based on Nernst-Planck equations or concentrated solution theories are often used to model similar electrochemical devices. Second-order differential equations systems with partial derivatives describe both the ion concentrations and the charge exchange processes occurring in the device. The application of these models was characterized by the limitations of charge storage and transport processes in the device due to diffusion. If the electrode material circulation and sufficiently fast charge transport are critical processes, then a sufficiently large diameter of the electrode flow channels is important. Otherwise, it is necessary to minimize the diameter of the same channel. At the same time, the experimental work showed that the phenomena caused by diffusion are critical side effects and have a significant effect on electrode charging processes. The models based on the Nernst-Planck equations and the stochastic model developed successfully matched the experimental results. Moreover, the developed stochastic model allows to simulate the convection and mixing processes of liquid electrodes successfully and to apply the effects of side reactions. Thus, the developed approach opens the possibility to find a solution to the central problem of the flow capacitor design – how to ensure sufficient flow of electrode material from the device and at the same time avoid limiting the transport of charge due to diffusion.

Due to the development of EFC technology, a significant increase in the storage capacity of energy from renewable sources can be expected. At the same time, to improve the power density of EFCs without compromising their high energy density and cyclicality, it is necessary to monitor the coherence of developments with other energy storage and conversion technologies. Important factors are the choice of operating conditions of the device, the design of the electrodes, the materials of the electrolyte, as well as suitable catalysts.

5. SUMMARY IN ESTONIAN

Elektrokeemilise voogkondensaatori arendamine ja optimiseerimine

Elektrokeemiline voogkondensaator (EFC) on kontseptuaalne lahendus elektrienergia mastaapseks salvestamiseks. Kõnealune seade sarnaneb tööpõhimõttelt superkondensaatorile, aga olulise erinevusena kasutab tahkete elektroodide asemel süsniniku mikro ja nano-osakestest ning elektrolüüdist koosnevat suspensiooni. Elektrolüüdiga suspensioon on eraldatud poorse, ioonjuhtiva membraaniga ja seadmes on tüüpiliselt mõne millimeetrilise diameetriga kanalid, mille sein on voolkollektoriks ning millest pumbatakse läbi eelpool kirjeldatud suspensiooni. Just nimelt süsinikupõhiste vedelate elektroodide kasutamine võimaldab arendatavat seadet olulisel määral skaleerida ning tulevikus integreerida olemasolevatesse elektrivõrkudesse ja/või rakendada seda efektiivselt taastuvate energiaallikate poolt toodetud elektrienergia salvestamiseks.

Doktoritöö keskseks eesmärgiks on EFC-tehnoloogia fundamentaalsete omaduste interpreteerimine. Sellest tulenevalt on töös on läbi viidud EFC elektrokeemilised karakteriseerimised ja arvutisimulatsioonid seadme disainlahenduste optimeerimiseks. Simulatsioonide valdkonnas on sobitatud EFC modelleerimiseks nii olemasolevaid elektrokeemilisi mudeled kui on arendatud ka uudne nn stohhastiline Monte-Carlo põhimõtetel baseeruv mudel. Väljatöötatud mudelid kalibreeriti ja valideeriti põhjalikult võrdluses elektrokeemiliste tulemustega ning neid kasutati voogelektroodide laadimisprotsessi sügavamaks mõistmiseks kolmes fundamentaalses EFC-seadme konstruktsioonis.

Sarnaste elektrokeemiliste seadmete modelleerimiseks kasutatakse tihti Nernst-Planki võrranditel või kontsentreeritud lahuse teooriatel baseeruvaid mudeleid. Luuakse teist järku osatuletsitega diferentsiaalvõrrandite süsteemid, mis kirjeldavad nii ioonide kontsentratsioone kui ka seadmes tekkivaid laenguülekande protsesse. Nende mudelite rakendamine iseloomustas ilmekalt difusiooni tõttu seadmes tekkivaid laengu salvestamise ja osakeste transpordi piiranguid. Efektiivne elektroodimaterjali tsirkulatsioon ning piisavalt kiire laengu transport on teineteisele vastanduvad protsessid – kui esimesel juhul on oluliseks näitajaks piisavalt suur elektroodi voolukanalite diameeter, siis teisel juhul on nõutav just nimelt sama kanali diameetri minimiseerimine. Samas ilmnes eksperimentaalsest tulemustest, et mitte ainult difusioonist tingitud nähtused pole olulised, vaid märkimisväärset mõju omavad ka nn kõrvalreaktsioonid. Töö käigus loodud stohhastiline mudel võimaldas saavutada edukalt elektrokeemiliste mõõtmistulemuste ning Nernst-Planki võrranditel baseeruvate mudelitega leitud tulemuste kokkulangevuse. Enamgi, loodud stohhastiline mudel võimaldab edukalt simuleerida vedelate elektroodide laadumise dünaamikat ja kirjeldada suspensioonis asetleidvaid protsesse ning hinnata kõrvalreaktsioonide mõjusid. Kokkuvõtvalt avab loodud lähenemisviis võimaluse leidmaks lahendust voogkondensaatori disaini kesksele probleemile – kuidas tagada seadmest piisav elektroodimaterjali läbivool ning samas hoiduda laengu transpordi limiteerimisest difusiooni tõttu.

EFC-tehnoloogia edasise arengu puhul võib eeldada taastuvatest allikatest toodetud energia salvestamisvõimsuse märkimisväärset kasvu. Samas tuleb lisada, et EFC võimsustiheduse parandamiseks, ilma et see kahjustaks nende seadmete energiatihedust ning tsükleeritavust, on vaja jälgida arenduste kooskõla ka muude energiasalvestus- ja muundamis-tehnoloogiatega. Olulisteks faktoriteks on nii seadme töötingimuste valik, elektroodide disain, elektrolüüdi materjalid, kuid samuti ka sobilikud katalüsaatorid.

6. ACKNOWLEDGMENT

Undertaking this Ph.D. has been a truly life-changing experience for me, and it would not have been possible to do without the support and guidance that I received from many people.

First of all, it is a genuine pleasure to express my deep sense of thanks and gratitude to my supervisors, Janno Torop, Veronika Zadin, and Alvo Aabloo. Their guidance, scholarly advice, and scientific approach have helped me to a very great extent to accomplish this task.

I am grateful to all my supportive colleagues from IMS Lab and MATTER who have helped me reach my goals.

Last but not least, I very much appreciate the continuous support from my beloved parents, sisters, and my friend for all those years.

Thank you all for making this journey special!

7. REFERENCES

[1]   S. Hameer, J.L. van Niekerk, A review of large-scale electrical energy storage, Int. J. Energy Res. 39 (2015) 1179–1195. https://doi.org/10.1002/ER.3294.

[2]   M.S. Whittingham, History, evolution, and future status of energy storage, Proc. IEEE. 100 (2012) 1518–1534. https://doi.org/10.1109/JPROC.2012.2190170.

[3]   E. Hittinger, J.F. Whitacre, J. Apt, What properties of grid energy storage are most valuable?, J. Power Sources. 206 (2012) 436–449. https://doi.org/10.1016/j.jpowsour.2011.12.003.

[4]   M. Winter, R.J. Brodd, What are batteries, fuel cells, and supercapacitors?, Chem. Rev. 104 (2004) 4245–4269. https://doi.org/10.1021/cr020730k.

[5]   Z. Liao, S. Zhang, K. Li, M. Zhao, Z. Qiu, D. Han, G. Zhang, T.G. Habetler, Hazard analysis of thermally abused lithium-ion batteries at different state of charges, J. Energy Storage. 27 (2020). https://doi.org/10.1016/j.est.2019.101065.

[6]   X. Han, X. Li, J. White, C. Zhong, Y. Deng, W. Hu, T. Ma, Metal-Air Batteries: From Static to Flow System, Adv. Energy Mater. (2018). https://doi.org/10.1002/aenm.201801396.

[7]   H. Zhang, S. Jeong, B. Qin, D. Vieira Carvalho, D. Buchholz, S. Passerini, Towards High-Performance Aqueous Sodium-Ion Batteries: Stabilizing the Solid/Liquid Interface for NASICON-Type $Na_2VTi(PO_4)_3$ using Concentrated Electrolytes, ChemSusChem. 11 (2018) 1382–1389. https://doi.org/10.1002/cssc.201800194.

[8]   T.J. Petek, N.C. Hoyt, R.F. Savinell, J.S. Wainright, Slurry electrodes for iron plating in an all-iron flow battery, J. Power Sources. 294 (2015) 620–626. https://doi.org/10.1016/j.jpowsour.2015.06.050.

[9]   A.K. Shukla, S. Sampath, K. Vijayamohanan, Electrochemical supercapacitors: Energy storage beyond batteries, Curr. Sci. 79 (2000).

[10]   V. Presser, C.R. Dennison, J. Campos, K.W. Knehr, E.C. Kumbur, Y. Gogotsi, The electrochemical flow capacitor: A new concept for rapid energy storage and recovery, Adv. Energy Mater. 2 (2012) 895–902. https://doi.org/10.1002/aenm.201100768.

[11]   B. Akuzum, P. Singh, D.A. Eichfeld, L. Agartan, S. Uzun, Y. Gogotsi, E.C. Kumbur, Percolation Characteristics of Conductive Additives for Capacitive Flowable (Semi-Solid) Electrodes, ACS Appl. Mater. Interfaces. 12 (2020) 5866–5875. https://doi.org/10.1021/acsami.9b19739.

[12]   S. Porada, J. Lee, D. Weingarth, V. Presser, Continuous operation of an electrochemical flow capacitor, Electrochem. Commun. 48 (2014) 178–181. https://doi.org/10.1016/j.elecom.2014.08.023.

[13]   J.W. Campos, Y. Gogotsi, Investigation of Electrode Materials for an Electrochemical Flow Capacitor, Chem. Biol. Eng. Masters of (2012).

[14]   J.W. Campos, M. Beidaghi, K.B. Hatzell, C.R. Dennison, B. Musci, V. Presser, E.C. Kumbur, Y. Gogotsi, Investigation of carbon materials for use as a flowable electrode in electrochemical flow capacitors, Electrochim. Acta. 98 (2013) 123–130. https://doi.org/10.1016/J.ELECTACTA.2013.03.037.

[15]   K.Y. Choo, C.Y. Yoo, M.H. Han, D.K. Kim, Electrochemical analysis of slurry electrodes for flow-electrode capacitive deionization, J. Electroanal. Chem. 806 (2017) 50–60. https://doi.org/10.1016/j.jelechem.2017.10.040.

[16]   C.Y. Foo, A. Sumboja, D.J.H. Tan, J. Wang, P.S. Lee, Flexible and highly scalable V2O5-rGO electrodes in an organic electrolyte for supercapacitor devices, Adv. Energy Mater. 4 (2014) 1400236. https://doi.org/10.1002/aenm.201400236.

[17]   H. Usui, Y. Domi, K. Fujiwara, M. Shimizu, T. Yamamoto, T. Nohira, R. Hagi-wara, H. Sakaguchi, Charge-Discharge Properties of a Sn4P3 Negative Electrode in Ionic Liquid Electrolyte for Na-Ion Batteries, ACS Energy Lett. 2 (2017) 1139–1143. https://doi.org/10.1021/acsenergylett.7b00252.

[18]   H. Srour, L. Chancelier, E. Bolimowska, T. Gutel, S. Mailley, H. Rouault, C.C. Santini, Ionic liquid-based electrolytes for lithium-ion batteries: review of performances of various electrode systems, J. Appl. Electrochem. 46 (2016) 149–155. https://doi.org/10.1007/s10800-015-0905-1.

[19]   N. Shukla, A.K. Thakur, Enhancement in electrical and stability properties of amorphous polymer based nanocomposite electrolyte, J. Non. Cryst. Solids. 357 (2011) 3689–3701. https://doi.org/10.1016/j.jnoncrysol.2011.06.036.

[20]   P. Yao, H. Yu, Z. Ding, Y. Liu, J. Lu, M. Lavorgna, J. Wu, X. Liu, Review on Polymer-Based Composite Electrolytes for Lithium Batteries, Front. Chem. 7 (2019) 522. https://doi.org/10.3389/fchem.2019.00522.

[21]   L.Q. Fan, Q.M. Tu, C.L. Geng, J.L. Huang, Y. Gu, J.M. Lin, Y.F. Huang, J.H. Wu, High energy density and low self-discharge of a quasi-solid-state supercapacitor with carbon nanotubes incorporated redox-active ionic liquid-based gel polymer electrolyte, Electrochim. Acta. 331 (2020) 135425. https://doi.org/10.1016/j.electacta.2019.135425.

[22]   T.J. Petek, N.C. Hoyt, R.F. Savinell, J.S. Wainright, Characterizing Slurry Electrodes Using Electrochemical Impedance Spectroscopy, J. Electrochem. Soc. 163 (2016) A5001–A5009. https://doi.org/10.1149/2.0011601jes.

[23]   M. Armand, J.M. Tarascon, Building better batteries, Nature. 451 (2008) 652–657. https://doi.org/10.1038/451652a.

[24]   Z. Lin, E. Goikolea, A. Balducci, K. Naoi, P.L. Taberna, M. Salanne, G. Yushin, P. Simon, Materials for supercapacitors: When Li-ion battery power is not enough, Mater. Today. 21 (2018) 419–436. https://doi.org/10.1016/j.mattod.2018.01.035.

[25]   E.W. Zhao, T. Liu, E. Jónsson, J. Lee, I. Temprano, R.B. Jethwa, A. Wang, H. Smith, J. Carretero-González, Q. Song, C.P. Grey, In situ NMR metrology reveals reaction mechanisms in redox flow batteries, Nature. 579 (2020) 224–228. https://doi.org/10.1038/s41586-020-2081-7.

[26]   Y. Zhang, J. Zhao, P. Wang, M. Skyllas-Kazacos, B. Xiong, R. Badrinarayanan, A comprehensive equivalent circuit model of all-vanadium redox flow battery for power system analysis, J. Power Sources. 290 (2015) 14–24. https://doi.org/10.1016/j.jpowsour.2015.04.169.

[27]   A.Y. Rychagov, N.A. Urisson, Y.M. Vol'fkovich, Electrochemical characteristics and properties of the surface of activated carbon electrodes in a double-layer capacitor, Russ. J. Electrochem. 37 (2001) 1172–1179. https://doi.org/10.1023/A:1012715615873.

[28]   S.C. Smith, P.K. Sen, Ultracapacitors and energy storage: Applications in electrical power system, in: 40th North Am. Power Symp. NAPS2008, 2008. https://doi.org/10.1109/NAPS.2008.5307299.

[29]   A. Burke, Ultracapacitors: Why, how, and where is the technology, J. Power Sources. 91 (2000) 37–50. https://doi.org/10.1016/S0378-7753(00)00485-7.

[30]   S.K. Kim, J. Cho, J.S. Moore, H.S. Park, P. V. Braun, High-Performance Meso-structured Organic Hybrid Pseudocapacitor Electrodes, Adv. Funct. Mater. 26 (2016) 903–910. https://doi.org/10.1002/adfm.201504307.

[31] D.P. Dubal, O. Ayyad, V. Ruiz, P. Gómez-Romero, Hybrid energy storage: The merging of battery and supercapacitor chemistries, Chem. Soc. Rev. 44 (2015) 1777–1790. https://doi.org/10.1039/c4cs00266k.

[32] A. Le Comte, Y. Reynier, C. Vincens, C. Leys, P. Azaïs, First prototypes of hybrid potassium-ion capacitor (KIC): An innovative, cost-effective energy storage technology for transportation applications, J. Power Sources. 363 (2017) 34–43. https://www.sciencedirect.com/science/article/pii/S0378775317308789 (accessed May 31, 2019).

[33] S. Roldán, D. Barreda, M. Granda, R. Menéndez, R. Santamaría, C. Blanco, An approach to classification and capacitance expressions in electrochemical capacitors technology, Phys. Chem. Chem. Phys. 17 (2015) 1084–1092. https://doi.org/10.1039/c4cp05124f.

[34] J.A. Staser, J.W. Weidner, Mathematical modeling of hybrid asymmetric electrochemical capacitors, in: J. Electrochem. Soc., 2014: pp. 3267–3275. https://doi.org/10.1149/2.031408jes.

[35] L. Kouchachvili, W. Yaïci, E. Entchev, Hybrid battery/supercapacitor energy storage system for the electric vehicles, J. Power Sources. 374 (2018) 237–248. https://doi.org/10.1016/j.jpowsour.2017.11.040.

[36] B. Akuzum, L. Agartan, J. Locco, E.C. Kumbur, Effects of particle dispersion and slurry preparation protocol on electrochemical performance of capacitive flowable electrodes, J. Appl. Electrochem. 47 (2017) 369–380. https://doi.org/10.1007/s10800-017-1046-5.

[37] N.C. Hoyt, E. Agar, E.A. Nagelli, R. Savinell, J. Wainright, Electrochemical Impedance Spectroscopy of Flowing Electrosorptive Slurry Electrodes, J. Electrochem. Soc. 165 (2018) E439–E444. https://doi.org/10.1149/2.0051810jes.

[38] H. Cohen, S.E. Eli, M. Jõgi, M.E. Suss, Suspension Electrodes Combining Slurries and Upflow Fluidized Beds, ChemSusChem. 9 (2016) 3045–3048. https://doi.org/10.1002/cssc.201601008.

[39] A.M. Johnson, J. Newman, Desalting by Means of Porous Carbon Electrodes, J. Electrochem. Soc. 118 (1971) 510–517. https://doi.org/10.1149/1.2408094.

[40] N.C. Hoyt, J.S. Wainright, R.F. Savinell, Mathematical Modeling of Electrochemical Flow Capacitors, J. Electrochem. Soc. 162 (2015) A652–A657. https://doi.org/10.1149/2.0411504jes.

[41] N.C. Hoyt, J.S. Wainright, R.F. Savinell, Current Density Scaling in Electrochemical Flow Capacitors, J. Electrochem. Soc. 162 (2015) 1102–1110. https://doi.org/10.1149/2.0031507jes.

[42] M. Karzar-Jeddi, H. Luo, P.T. Cummings, K.B. Hatzell, Computational Modeling of Particle Hydrodynamics and Charging Process for the Flowable Electrodes of Carbon Slurry, J. Electrochem. Soc. 166 (2019) A2643–A2653. https://doi.org/10.1149/2.1191912jes.

[43] A.C. Forse, C. Merlet, J.M. Griffin, C.P. Grey, New perspectives on the charging mechanisms of supercapacitors, J. Am. Chem. Soc. 138 (2016) 5731–5744. https://doi.org/10.1021/jacs.6b02115.

[44] J. Lohaus, D. Rall, M. Kruse, V. Steinberger, M. Wessling, On charge percolation in slurry electrodes used in vanadium redox flow batteries, Electrochem. Commun. 101 (2019) 104–108. https://doi.org/10.1016/j.elecom.2019.02.013.

[45] C. Lin, B.N. Popov, H.J. Ploehn, Modeling the Effects of Electrode Composition and Pore Structure on the Performance of Electrochemical Capacitors, J. Electrochem. Soc. 149 (2002) A167. https://doi.org/10.1149/1.1431575.

[46]   J. Torop, F. Summer, V. Zadin, T. Koiranen, A. Jänes, E. Lust, A. Aabloo, Low concentrated carbonaceous suspensions assisted with carboxymethyl cellulose as electrode for electrochemical flow capacitor, Eur. Phys. J. E. 42 (2019). https://doi.org/10.1140/epje/i2019-11766-2.

[47]   N.C. Hoyt, R.F. Savinell, J.S. Wainright, Modeling of flowable slurry electrodes with combined faradaic and nonfaradaic currents, Chem. Eng. Sci. 144 (2016) 288–297. https://doi.org/10.1016/j.ces.2016.01.048.

[48]   F. Summer, V. Zadin, S.S. Nakshatharan, A. Aabloo, J. Torop, Optimization of Electrochemical Flow Capacitor (EFC) design via finite element modeling, J. Energy Storage. 29 (2020) 101304. https://doi.org/10.1016/j.est.2020.101304.

[49]   C. Merlet, D.T. Limmer, M. Salanne, R. Van Roij, P.A. Madden, D. Chandler, B. Rotenberg, The Electric Double Layer Has a Life of Its Own, J. Phys. Chem. C. 118 (2014) 18291–18298. https://doi.org/10.1021/JP503224W.

[50]   L. Ma, L. Huang, Y. Xu, C. Liu, F. Wang, H. Xing, S. Ma, Dynamics and Model Research on the Electrosorption by Activated Carbon Fiber Electrodes, Water 2021, Vol. 13, Page 62. 13 (2020) 62. https://doi.org/10.3390/W13010062.

[51]   G. Feng, S. Li, J.S. Atchison, V. Presser, P.T. Cummings, Molecular insights into carbon nanotube supercapacitors: Capacitance independent of voltage and temperature, J. Phys. Chem. C. 117 (2013) 9178–9186. https://doi.org/10.1021/jp403547k.

[52]   V. Ramadesigan, P.W.C. Northrop, S. De, S. Santhanagopalan, R.D. Braatz, V.R. Subramanian, Modeling and Simulation of Lithium-Ion Batteries from a Systems Engineering Perspective, J. Electrochem. Soc. 159 (2012) R31–R45. https://doi.org/10.1149/2.018203jes.

[53]   J.K. McDonough, A.I. Frolov, V. Presser, J. Niu, C.H. Miller, T. Ubieto, M. V. Fedorov, Y. Gogotsi, Influence of the structure of carbon onions on their electrochemical performance in supercapacitor electrodes, Carbon N. Y. 50 (2012) 3298–3309. https://doi.org/10.1016/J.CARBON.2011.12.022.

[54]   V.E. Brunini, Y.M. Chiang, W.C. Carter, Modeling the hydrodynamic and electrochemical efficiency of semi-solid flow batteries, Electrochim. Acta. 69 (2012) 301–307. https://doi.org/10.1016/j.electacta.2012.03.006.

[55]   C.R. Dennison, Y. Gogotsi, E.C. Kumbur, In situ distributed diagnostics of flowable electrode systems: Resolving spatial and temporal limitations, Phys. Chem. Chem. Phys. 16 (2014) 18241–18252. https://doi.org/10.1039/c4cp02820a.

[56]   Z.Y. Liu, J.L. Zhang, P.T. Yu, J.X. Zhang, R. Makharia, K.L. More, E.A. Stach, Transmission Electron Microscopy Observation of Corrosion Behaviors of Platinized Carbon Blacks under Thermal and Electrochemical Conditions, J. Electrochem. Soc. 157 (2010) B906. https://doi.org/10.1149/1.3391737.

[57]   T. Maiyalagan, T.O. Alaje, K. Scott, Highly Stable Pt–Ru Nanoparticles Supported on Three-Dimensional Cubic Ordered Mesoporous Carbon (Pt–Ru/CMK-8) as Promising Electrocatalysts for Methanol Oxidation, J. Phys. Chem. C. 116 (2012) 2630–2638. https://doi.org/10.1021/JP210266N.

[58]   V. Srinivasan, J.W. Weidner, Mathematical Modeling of Electrochemical Capacitors, J. Electrochem. Soc. 146 (1999) 1650. https://doi.org/10.1149/1.1391821.

[59]   M. O. Bamgbopa, Dagmawi Belaineh, D. A. Mengistie, Jesper Edberg, Isak Engquist, Magnus Berggren, Klas Tybrandt, Modelling of heterogeneous ion transport in conducting polymer supercapacitors, J. Mater. Chem. A. 9 (2021) 2184–2194. https://doi.org/10.1039/D0TA09429C.

[60] N.C. Hoyt, J.S. Wainright, R.F. Savinell, Mathematical Modeling of Electro-chemical Flow Capacitors, J. Electrochem. Soc. 162 (2015) A652–A657. https://doi.org/10.1149/2.0411504jes.

[61] J.S. Newman, C.W. Tobias, Theoretical Analysis of Current Distribution in Porous Electrodes, J. Electrochem. Soc. 109 (1962) 1183–1191. https://doi.org/10.1149/1.2425269.

[62] G. Madabattula, S.K. Gupta, Modeling of Supercapacitor, Comsol Conf. (2012).

[63] R. Memming, R. Memming, Electrochemical Systems, in: Semicond. Electro-chem., J. Wiley, 2015: pp. 49–64. https://doi.org/10.1002/9783527688685.ch3.

[64] A. Schmidt, E. Ramani, T. Carraro, J. Joos, A. Weber, M. Kamlah, E. Ivers-Tiffée, Understanding Deviations between Spatially Resolved and Homogenized Cathode Models of Lithium-Ion Batteries, Energy Technol. 9 (2021) 2000881. https://doi.org/10.1002/ENTE.202000881.

[65] C.A. Emereuwa, Mathematical homogenization and stochastic modeling of energy storage systems, Curr. Opin. Electrochem. 21 (2020) 117–124. https://doi.org/10.1016/J.COELEC.2020.01.009.

[66] C.H. Hesse, E. Ramos, Dynamic simulation of a stochastic model for particle sedimentation in fluids, Appl. Math. Model. 18 (1994) 437–445. https://doi.org/10.1016/0307-904X(94)90305-0.

[67] L. Lu, K. Yoo, S. Benyahia, Coarse-Grained-Particle Method for Simulation of Liquid-Solids Reacting Flows, Ind. Eng. Chem. Res. 55 (2016) 10477–10491. https://doi.org/10.1021/acs.iecr.6b02688.

[68] A. Castellanos, A. Ramos, A. González, N.G. Green, H. Morgan, Electrohydro-dynamics and dielectrophoresis in microsystems: scaling laws, J. Phys. D. Appl. Phys. 36 (2003) 2584. https://doi.org/10.1088/0022-3727/36/20/023.

[69] G. Eslami, E. Esmaeilzadeh, A.T. Pérez, Modeling of conductive particle motion in viscous medium affected by an electric field considering particle-electrode interactions and microdischarge phenomenon, Phys. Fluids. 28 (2016). https://doi.org/10.1063/1.4964683.

[70] B. Çetin, S.D. Öner, B. Baranoğlu, Modeling of dielectrophoretic particle motion: Point particle versus finite-sized particle, Electrophoresis. 38 (2017) 1407–1418. https://doi.org/10.1002/elps.201600461.

[71] E. V Romashchenko, A.A. Bizyukov, I.O. Girka, Dynamics of macroparticle in a weakly collisional plasma, Probl. At. Sci. Technol. 119 (2019) 112–115.

[72] T.Z. Esirkepov, Exact charge conservation scheme for Particle-in-Cell simulation with an arbitrary form-factor, Comput. Phys. Commun. 135 (2001) 144–153. https://doi.org/10.1016/S0010-4655(00)00228-9.

[73] S. Santhanagopalan, Q. Guo, R.E. White, Parameter Estimation and Model Discrimination for a Lithium-Ion Cell, J. Electrochem. Soc. 154 (2007) A198. https://doi.org/10.1149/1.2422896.

[74] V. Boovaragavan, S. Harinipriya, V.R. Subramanian, Towards real-time (milli-seconds) parameter estimation of lithium-ion batteries using reformulated physics-based models, J. Power Sources. 183 (2008) 361–365. https://doi.org/10.1016/j.jpowsour.2008.04.077.

[75] M.J.D. Powell, The BOBYQA algorithm for bound constrained optimization with-out derivatives, NA Rep. NA2009/06. (2009) 1–39. https://doi.org/10.1.1.443.7693.

[76]   M. Li, H.H. Hu, H.H. Bau, Capacitive charging and desalination dynamics of a packed-bed reactor, Phys. Chem. Chem. Phys. 17 (2015) 7181–7195. https://doi.org/10.1039/C4CP05240D.

[77]   H.S. Fricker, Why does charge concentrate on points?, Phys. Educ. 24 (1989) 157–161. https://doi.org/10.1088/0031-9120/24/3/309.

[78]   C. Portet, P.. Taberna, P. Simon, C. Laberty-Robert, Modification of Al current collector surface by sol–gel deposit for carbon–carbon supercapacitor applications, Electrochim. Acta. 49 (2004) 905–912. https://doi.org/10.1016/J.ELECTACTA.2003.09.043.

[79]   A. Martín-Molina, M. Quesada-Pérez, F. Galisteo-González, R. Hidalgo-Álvarez, Looking into overcharging in model colloids through electrophoresis: Asymmetric electrolytes, J. Chem. Phys. 118 (2003) 4183–4189. https://doi.org/10.1063/1.1540631.

[80]   A. Martín-Molina, M. Quesada-Pérez, F. Galisteo-González, R. Hidalgo-Álvarez, Primitive models and electrophoresis: An experimental study, in: Colloids Surfaces A Physicochem. Eng. Asp., 2003: pp. 155–164. https://doi.org/10.1016/S0927-7757(03)00254-1.

[81]   P.L. Johnson, Predicting the impact of particle-particle collisions on turbophoresis with a reduced number of computational particles, Int. J. Multiph. Flow. 124 (2020) 103182. https://doi.org/10.1016/j.ijmultiphaseflow.2019.103182.

[82]   R. Garg, C. Narayanan, S. Subramaniam, A numerically convergent Lagrangian–Eulerian simulation method for dispersed two-phase flows, Int. J. Multiph. Flow. 35 (2009) 376–388. https://doi.org/10.1016/J.IJMULTIPHASEFLOW.2008.12.004.

[83]   A.I. Momot, A.G. Zagorodny, I.S. Orel, Interaction force between two finite-size charged particles in weakly ionized plasma, Phys. Rev. E. 95 (2017) 13212. https://doi.org/10.1103/PhysRevE.95.013212.

[84]   S. Cloete, S.T. Johansen, S. Amini, Grid independence behaviour of fluidized bed reactor simulations using the Two Fluid Model: Effect of particle size, Powder Technol. 269 (2015) 153–165. https://doi.org/10.1016/j.powtec.2014.08.055.

[85]   V. Verma, J.T. Padding, A novel approach to MP-PIC: Continuum particle model for dense particle flows in fluidized beds, Chem. Eng. Sci. X. 6 (2020) 100053. https://doi.org/10.1016/j.cesx.2019.100053.

8. PUBLICATIONS

9. CURRICULUM VITAE

Name: Faiza Summer
Date of birth: July 24, 1989
Citizenship: Pakistan
E-mail: faizasummer15@gmail.com , faiza.summer@ut.ee

Education:

2016–	University of Tartu, Faculty of Science and Technology, Ph.D.
2011–2013	International Islamic University Islamabad (IIUI), Department of Physics, MS.
2007–2011	University of Wah, Wah Cantt, Department of Physics, BS.

Work experience:

May 2021 – to Date	Simulation Engineer, Estonian Aviation Academy, Estonia.
Nov 2013 – June 2014	Lecturer Physics, Indus College of Science and Commerce, Wah Cantt, Pakistan.
Class of 2012	Physics Teacher, WISE School and College for Boys, Wah Cantt, Pakistan.
Class of 2010 & 2011	Physics Lecturer, Community Model College, Taxila, Pakistan.

DISSERTATIONES TECHNOLOGIAE
UNIVERSITATIS TARTUENSIS

1. **Imre Mäger**. Characterization of cell-penetrating peptides: Assessment of cellular internalization kinetics, mechanisms and bioactivity. Tartu 2011, 132 p.
2. **Taavi Lehto**. Delivery of nucleic acids by cell-penetrating peptides: application in modulation of gene expression. Tartu 2011, 155 p.
3. **Hannes Luidalepp**. Studies on the antibiotic susceptibility of *Escherichia coli*. Tartu 2012, 111 p.
4. **Vahur Zadin**. Modelling the 3D-microbattery. Tartu 2012, 149 p.
5. **Janno Torop**. Carbide-derived carbon-based electromechanical actuators. Tartu 2012, 113 p.
6. **Julia Suhorutšenko**. Cell-penetrating peptides: cytotoxicity, immunogenicity and application for tumor targeting. Tartu 2012, 139 p.
7. **Viktoryia Shyp**. G nucleotide regulation of translational GTPases and the stringent response factor RelA. Tartu 2012, 105 p.
8. **Mardo Kõivomägi**. Studies on the substrate specificity and multisite phosphorylation mechanisms of cyclin-dependent kinase Cdk1 in *Saccharomyces cerevisiae*. Tartu, 2013, 157 p.
9. **Liis Karo-Astover**. Studies on the Semliki Forest virus replicase protein nsP1. Tartu, 2013, 113 p.
10. **Piret Arukuusk**. NickFects–novel cell-penetrating peptides. Design and uptake mechanism. Tartu, 2013, 124 p.
11. **Piret Villo**. Synthesis of acetogenin analogues. Asymmetric transfer hydrogenation coupled with dynamic kinetic resolution of α-amido-β-keto esters. Tartu, 2013, 151 p.
12. **Villu Kasari**. Bacterial toxin-antitoxin systems: transcriptional cross-activation and characterization of a novel *mqsRA* system. Tartu, 2013, 108 p.
13. **Margus Varjak**. Functional analysis of viral and host components of alphavirus replicase complexes. Tartu, 2013, 151 p.
14. **Liane Viru**. Development and analysis of novel alphavirus-based multi-functional gene therapy and expression systems. Tartu, 2013, 113 p.
15. **Kent Langel**. Cell-penetrating peptide mechanism studies: from peptides to cargo delivery. Tartu, 2014, 115 p.
16. **Rauno Temmer**. Electrochemistry and novel applications of chemically synthesized conductive polymer electrodes. Tartu, 2014, 206 p.
17. **Indrek Must**. Ionic and capacitive electroactive laminates with carbonaceous electrodes as sensors and energy harvesters. Tartu, 2014, 133 p.
18. **Veiko Voolaid**. Aquatic environment: primary reservoir, link, or sink of antibiotic resistance? Tartu, 2014, 79 p.
19. **Kristiina Laanemets**. The role of SLAC1 anion channel and its upstream regulators in stomatal opening and closure of *Arabidopsis thaliana.* Tartu, 2015, 115 p.

20. **Kalle Pärn**. Studies on inducible alphavirus-based antitumour strategy mediated by site-specific delivery with activatable cell-penetrating peptides. Tartu, 2015, 139 p.
21. **Anastasia Selyutina**. When biologist meets chemist: a search for HIV-1 inhibitors. Tartu, 2015, 172 p.
22. **Sirle Saul**. Towards understanding the neurovirulence of Semliki Forest virus. Tartu, 2015, 136 p.
23. **Marit Orav**. Study of the initial amplification of the human papillomavirus genome. Tartu, 2015, 132 p.
24. **Tormi Reinson**. Studies on the Genome Replication of Human Papillomaviruses. Tartu, 2016, 110 p.
25. **Mart Ustav Jr**. Molecular Studies of HPV-18 Genome Segregation and Stable Replication. Tartu, 2016, 152 p.
26. **Margit Mutso**. Different Approaches to Counteracting Hepatitis C Virus and Chikungunya Virus Infections. Tartu, 2016, 184 p.
27. **Jelizaveta Geimanen**. Study of the Papillomavirus Genome Replication and Segregation. Tartu, 2016, 168 p.
28. **Mart Toots**. Novel Means to Target Human Papillomavirus Infection. Tartu, 2016, 173 p.
29. **Kadi-Liis Veiman**. Development of cell-penetrating peptides for gene delivery: from transfection in cell cultures to induction of gene expression *in vivo*. Tartu, 2016, 136 p.
30. **Ly Pärnaste**. How, why, what and where: Mechanisms behind CPP/cargo nanocomplexes. Tartu, 2016, 147 p.
31. **Age Utt**. Role of alphavirus replicase in viral RNA synthesis, virus-induced cytotoxicity and recognition of viral infections in host cells. Tartu, 2016, 183 p.
32. **Veiko Vunder**. Modeling and characterization of back-relaxation of ionic electroactive polymer actuators. Tartu, 2016, 154 p.
33. **Piia Kivipõld**. Studies on the Role of Papillomavirus E2 Proteins in Virus DNA Replication. Tartu, 2016, 118 p.
34. **Liina Jakobson**. The roles of abscisic acid, CO_2, and the cuticle in the regulation of plant transpiration. Tartu, 2017, 162 p.
35. **Helen Isok-Paas**. Viral-host interactions in the life cycle of human papillomaviruses. Tartu, 2017, 158 p.
36. **Hanna Hõrak**. Identification of key regulators of stomatal CO_2 signalling via O_3-sensitivity. Tartu, 2017, 260 p.
37. **Jekaterina Jevtuševskaja**. Application of isothermal amplification methods for detection of *Chlamydia trachomatis* directly from biological samples. Tartu, 2017, 96 p.
38. **Ülar Allas**. Ribosome-targeting antibiotics and mechanisms of antibiotic resistance. Tartu, 2017, 152 p.
39. **Anton Paier**. Ribosome Degradation in Living Bacteria. Tartu, 2017, 108 p.
40. **Vallo Varik**. Stringent Response in Bacterial Growth and Survival. Tartu, 2017, 101 p.

41. **Pavel Kudrin**. In search for the inhibitors of *Escherichia coli* stringent response factor RelA. Tartu, 2017, 138 p.

42. **Liisi Henno**. Study of the human papillomavirus genome replication and oligomer generation. Tartu, 2017, 144 p.

43. **Katrin Krõlov**. Nucleic acid amplification from crude clinical samples exemplified by *Chlamydia trachomatis* detection in urine. Tartu, 2018, 118 p.

44. **Eve Sankovski**. Studies on papillomavirus transcription and regulatory protein E2. Tartu, 2018, 113 p.

45. **Morteza Daneshmand**. Realistic 3D Virtual Fitting Room. Tartu, 2018, 233 p.

46. **Fatemeh Noroozi**. Multimodal Emotion Recognition Based Human-Robot Interaction Enhancement. Tartu, 2018, 113 p.

47. **Krista Freimann**. Design of peptide-based vector for nucleic acid delivery in vivo. Tartu, 2018, 103 p.

48. **Rainis Venta**. Studies on signal processing by multisite phosphorylation pathways of the *S. cerevisiae* cyclin-dependent kinase inhibitor Sic1. Tartu, 2018, 155 p.

49. **Inga Põldsalu**. Soft actuators with ink-jet printed electrodes. Tartu, 2018, 85 p.

50. **Kadri Künnapuu**. Modification of the cell-penetrating peptide PepFect14 for targeted tumor gene delivery and reduced toxicity. Tartu, 2018, 114 p.

51. **Toomas Mets**. RNA fragmentation by MazF and MqsR toxins of *Escherichia coli.* Tartu, 2019, 119 p.

52. **Kadri Tõldsepp**. The role of mitogen-activated protein kinases MPK4 and MPK12 in CO_2-induced stomatal movements. Tartu, 2019, 259 p.

53. **Pirko Jalakas**. Unravelling signalling pathways contributing to stomatal conductance and responsiveness. Tartu, 2019, 120 p.

54. **S. Sunjai Nakshatharan**. Electromechanical modelling and control of ionic electroactive polymer actuators. Tartu, 2019, 165 p.

55. **Eva-Maria Tombak**. Molecular studies of the initial amplification of the oncogenic human papillomavirus and closely related nonhuman primate papillomavirus genomes. Tartu, 2019, 150 p.

56. **Meeri Visnapuu**. Design and physico-chemical characterization of metal-containing nanoparticles for antimicrobial coatings. Tartu, 2019, 138 p.

57. **Jelena Beljantseva**. Small fine-tuners of the bacterial stringent response – a glimpse into the working principles of Small Alarmone Synthetases. Tartu, 2020, 104 p.

58. **Egon Urgard**. Potential therapeutic approaches for modulation of inflammatory response pathways. Tartu, 2020, 120 p.

59. **Sofia Raquel Alves Oliveira**. HPLC analysis of bacterial alarmone nucleotide (p)ppGpp and its toxic analogue ppApp. Tartu, 2020, 122 p.

60. **Mihkel Örd**. Ordering the phosphorylation of cyclin-dependent kinase Cdk1 substrates in the cell cycle. Tartu, 2021, 228 p.

61. **Fred Elhi.** Biocompatible ionic electromechanically active polymer actuator based on biopolymers and non-toxic ionic liquids. Tartu, 2021, 140 p.
62. **Liisi Talas.** Reconstructing paleo-diversity, dynamics and response of eukaryotes to environmental change over the Late-Glacial and Holocene period in lake Lielais Svētiņu using sedaDNA. Tartu, 2021, 118 p.
63. **Livia Matt.** Novel isosorbide-based polymers. Tartu, 2021, 118 p.
64. **Koit Aasumets.** The dynamics of human mitochondrial nucleoids within the mitochondrial network. Tartu, 2021, 104 p.